Science Advances
AAAS

Supplementary Materials for

Discovery of distinct lithosphere-asthenosphere boundary and the Gutenberg discontinuity in the Atlantic Ocean

Pranav Audhkhasi and Satish C. Singh

Corresponding author: Satish C. Singh, singh@ipgp.fr

Sci. Adv. **8**, eabn5404 (2022)
DOI: 10.1126/sciadv.abn5404

This PDF file includes:

Figs. S1 to S31

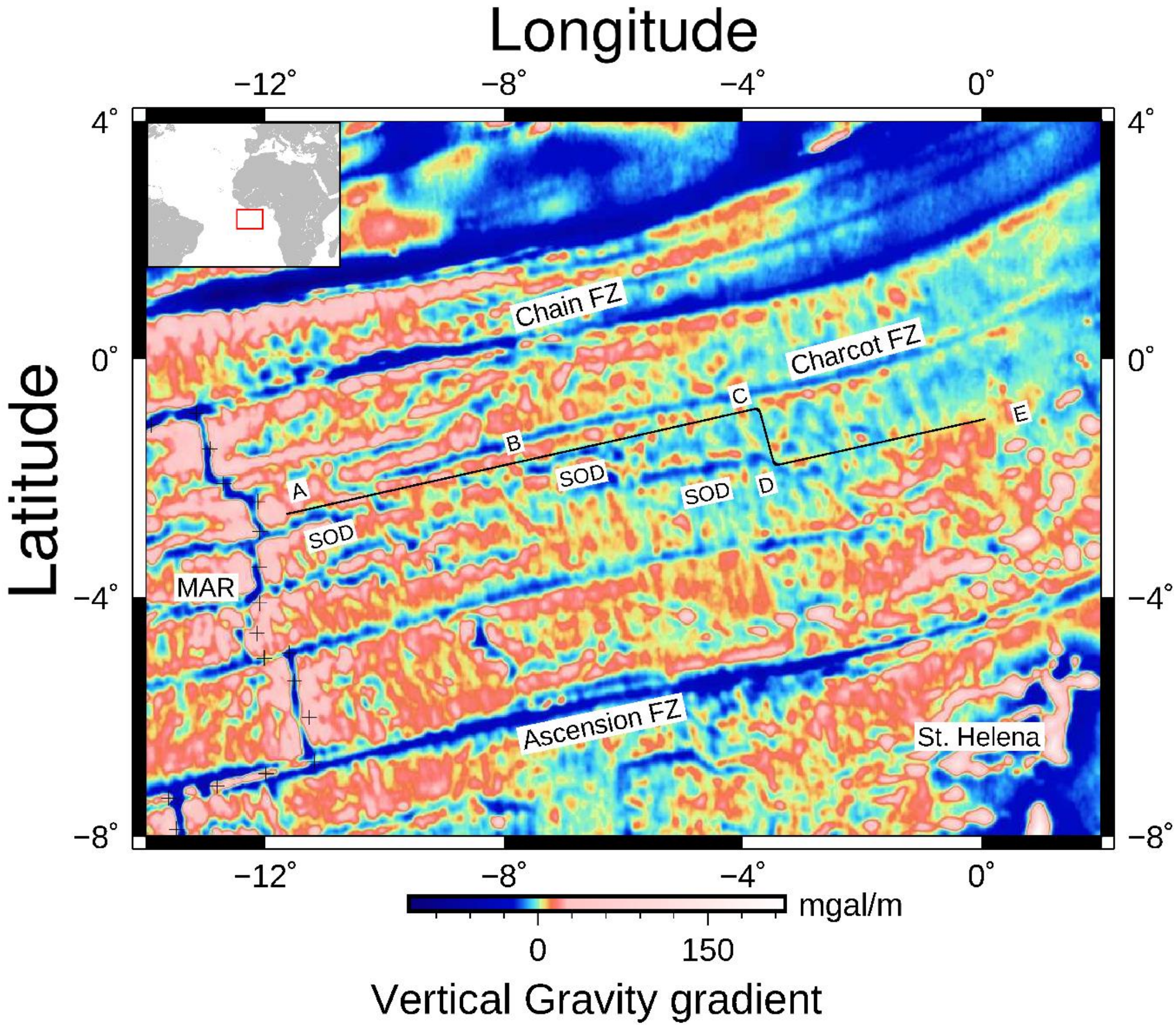

Fig. S1. Vertical gravity gradient map of the study region. Map showing the vertical gravity gradient (*41*) to highlight the second-order discontinuities (marked as SOD) near the profile. Seismic profile is marked in black (ABCDE). + indicates the Mid-Atlantic Ridge (MAR).

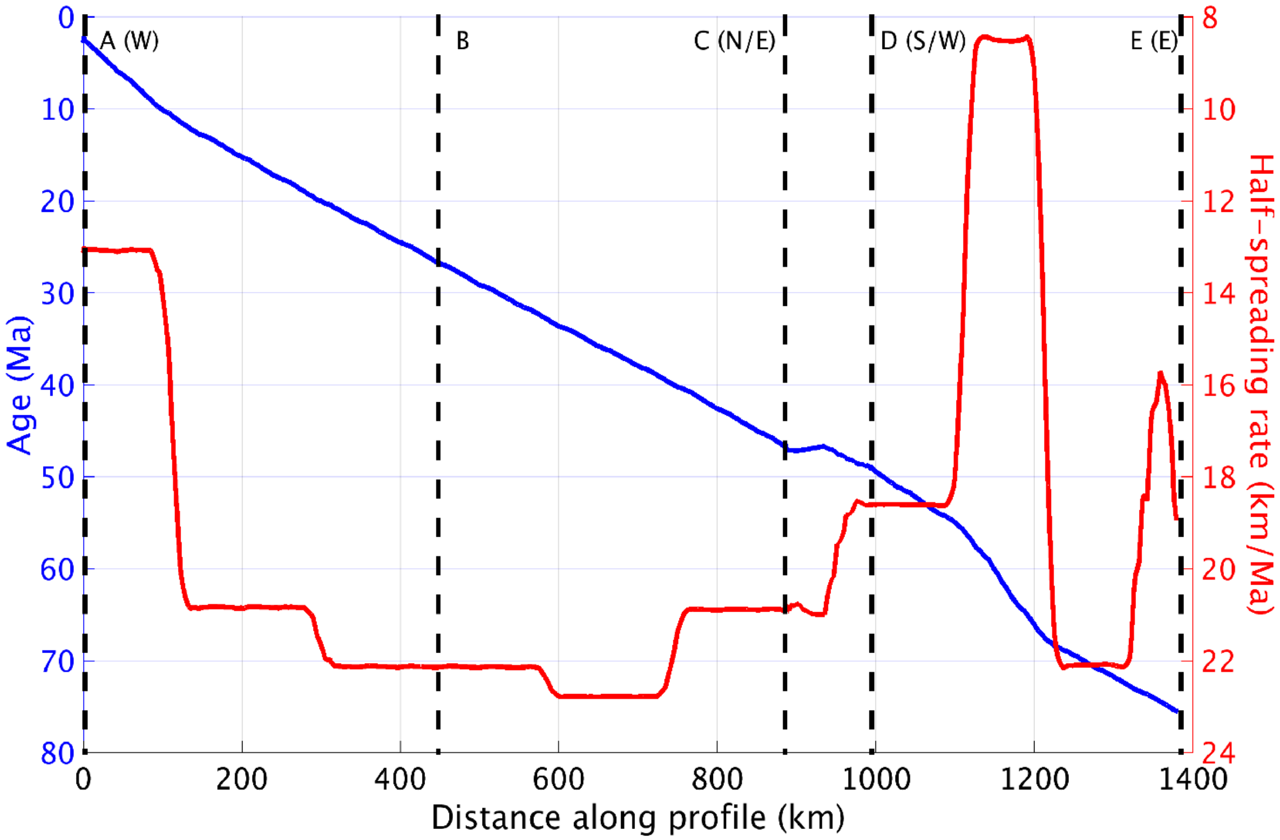

Fig. S2. Seafloor age and half-spreading. The seafloor age (*14*) is represented in blue and the half-spreading rate (*14*) in red along the profile with the dashed black vertical lines demarcating the segments of the profile. For the positions of A, B, C, D and E see fig. S1.

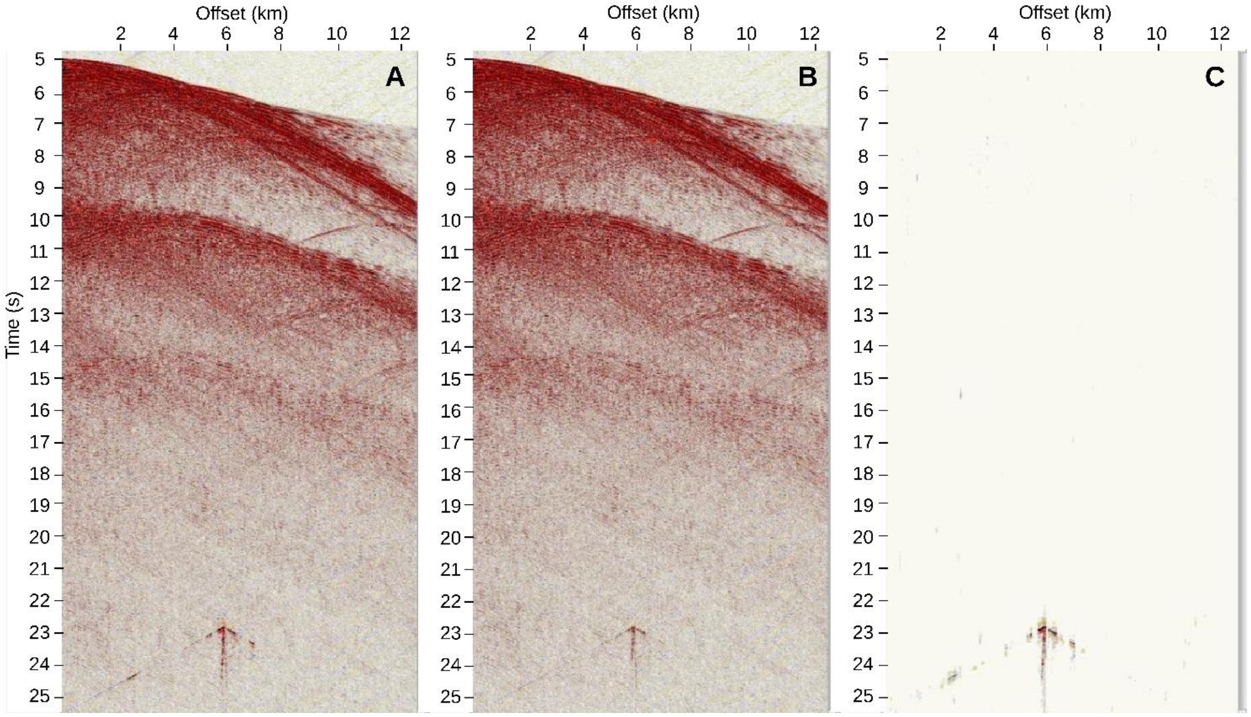

Fig. S3. Anomalous Amplitude Attenuation. (A) Original shot gather, (B) processed shot gather and (C) the difference between (A) and (B). The amplitude spike at 22.5 s has been attenuated. Amplitudes in all the panels are the same.

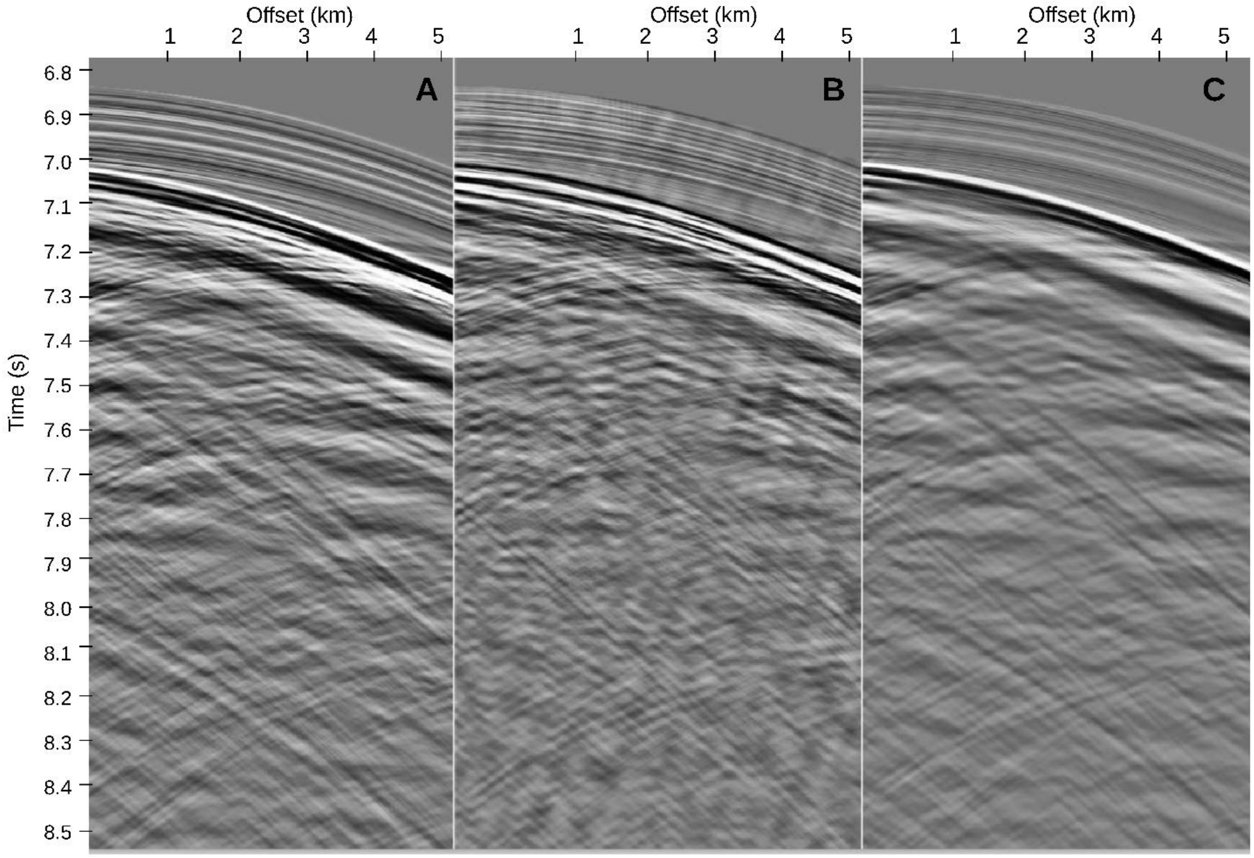

Fig. S4. Optimal de-ghosting by P-V_z summation. (A) Pressure component (*P*), (B) Vertical-velocity component (V_z), and (C) the summation of the two components (*40*). The reverberation around 6.9-7 s has been greatly reduced resulting in an enhanced frequency bandwidth. Amplitudes are uniform in all the panels.

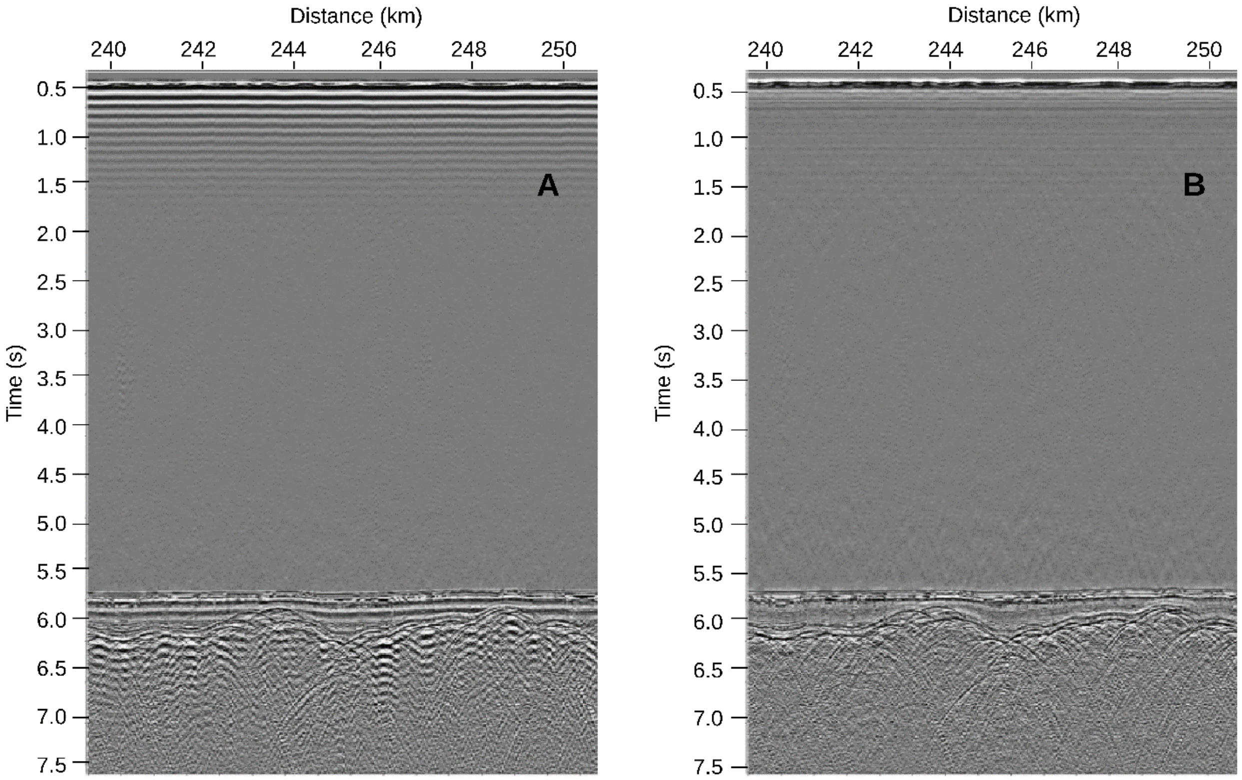

Fig. S5. Source signature de-bubble. Stack section showing the seafloor and basement before (A) and after (B) the marine source signature de-bubble. The source signature de-bubble was performed for each sources. Uniform amplitudes in both panels.

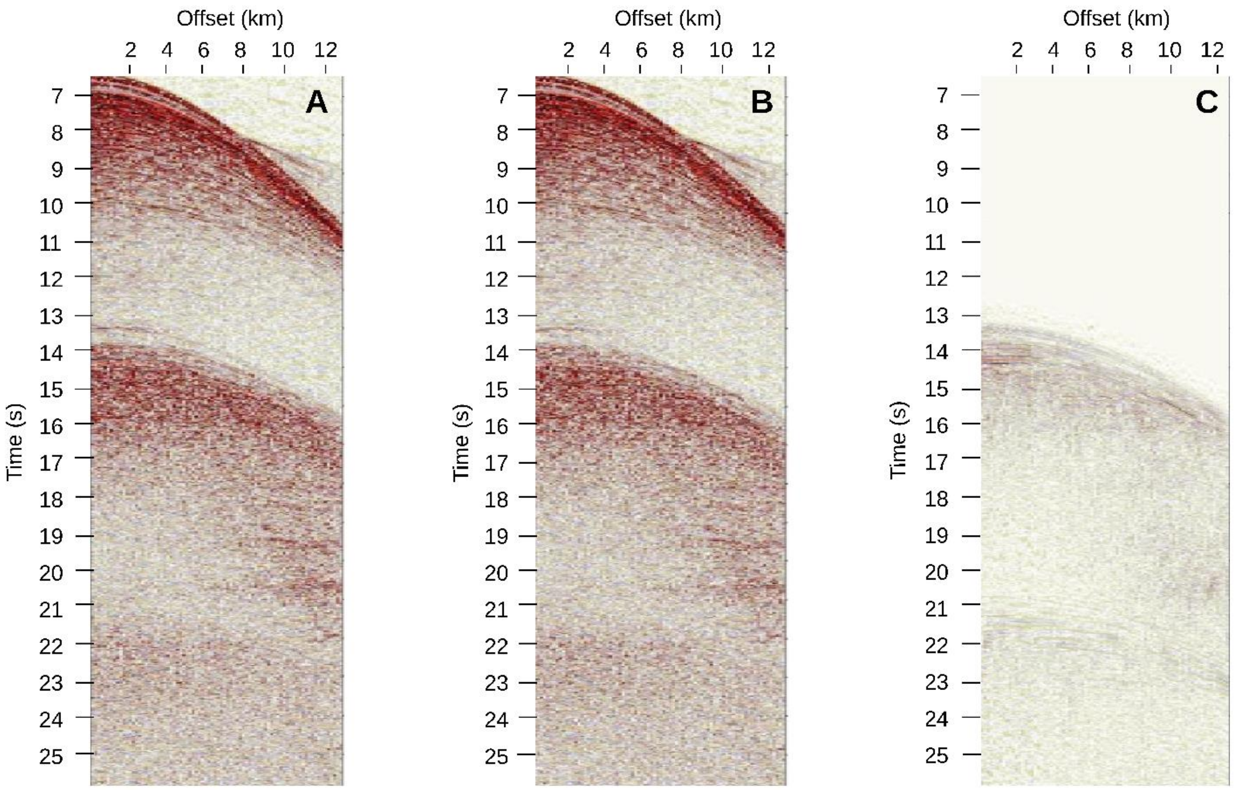

Fig. S6. De-multiple by Generalized Surface Related Multiple Elimination. (A) Shot gather before de-multiple, (B) the same shot gather after de-multiple by generalized surface related multiple prediction (*42*) and (C) the difference between (A) and (B). Amplitudes in all the panels are uniform.

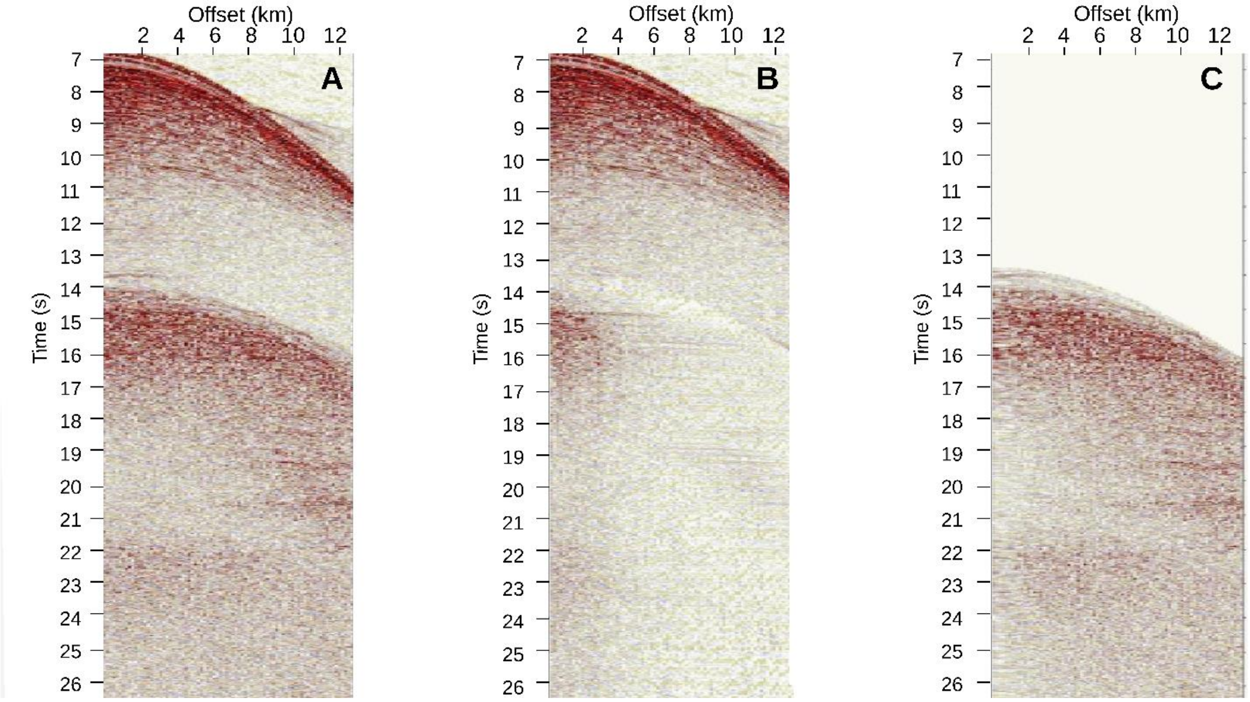

Fig. S7. De-multiple by weighted least squares radon. (A) Shot gather before de-multiple, (B) the same shot gather after de-multiple by weighted least squares Radon multiple removal and (C) the difference between (A) and (B). Amplitudes in all the panels are the same.

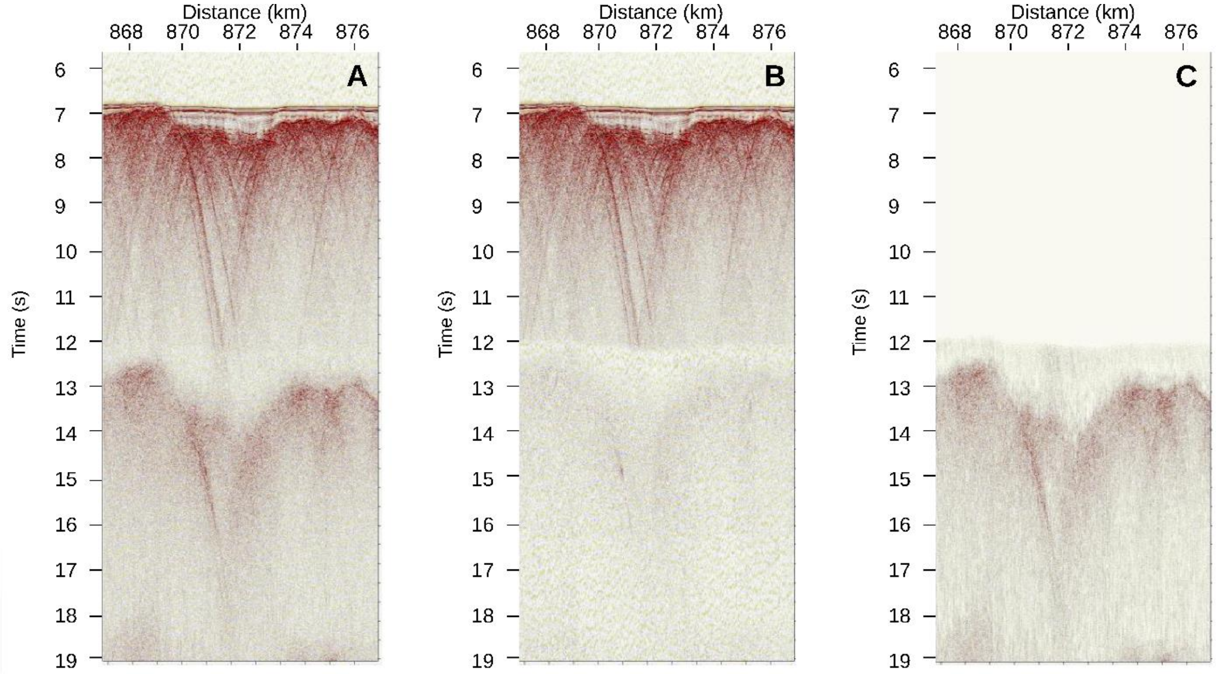

Fig. S8. De-multiple by post-Radon isolating multiple. (A) Stack section before de-multiple, (B) the same stack section after de-multiple by post-Radon isolating multiple and (C) the difference between (A) and (B). Amplitudes in all the panels are uniform.

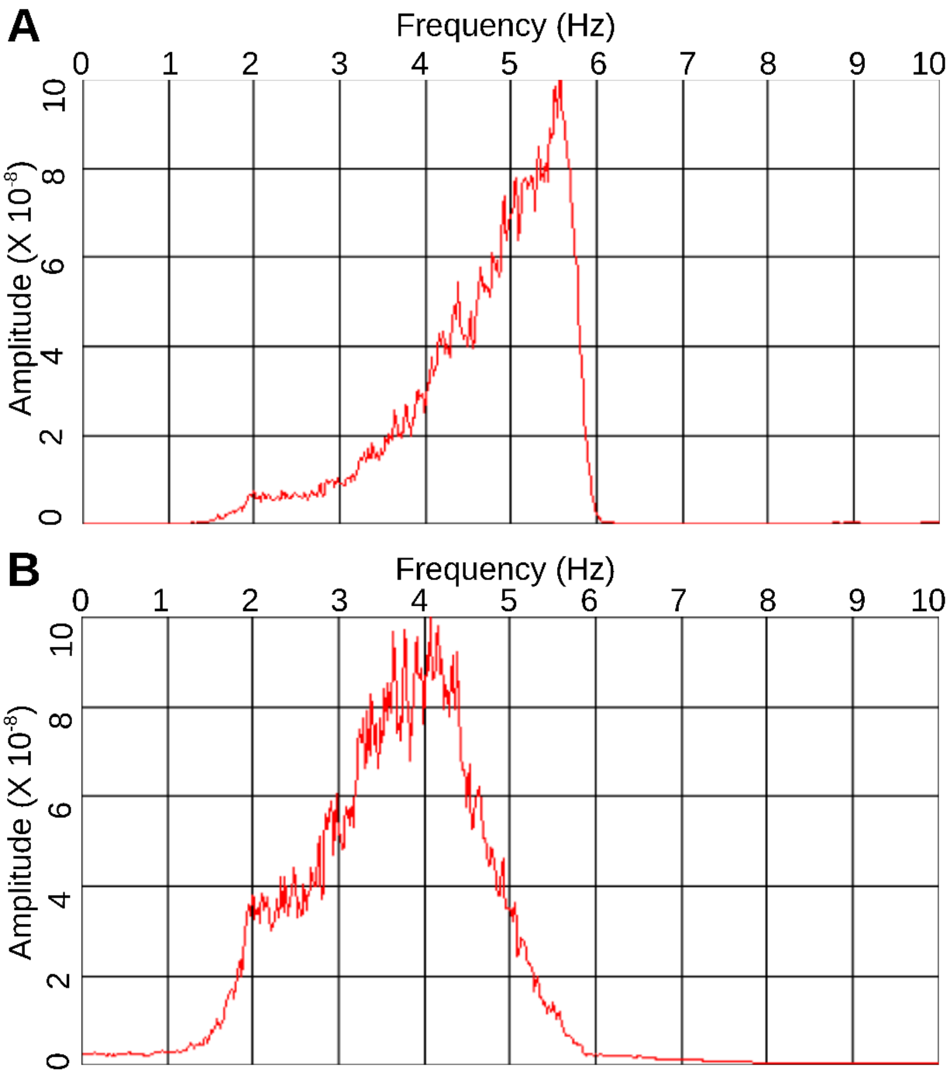

Fig. S9. Low-frequency enhancement. (A) The frequency spectrum of a shot gather after applying a band-pass filter from 1.5-5 Hz. (B) The frequency spectrum of the same shot gather after enhancing low frequencies from 2-5 Hz (*44*).

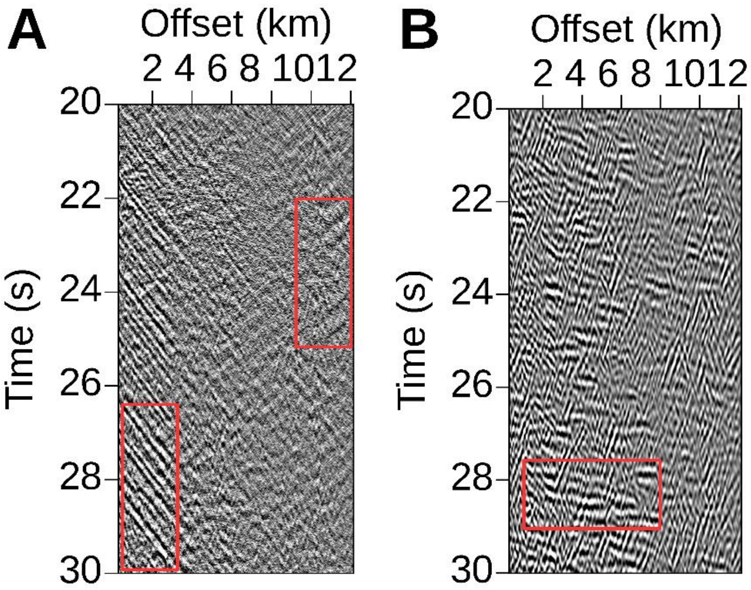

Fig. S10. Linear noise removal in shot-offset domain. (A) Shot gather after low frequency enhancement showing strong positively and negatively dipping linear noises (highlighted by windows). (B) The same shot gather after the removal of the linear dipping noise (window highlights the reflection).

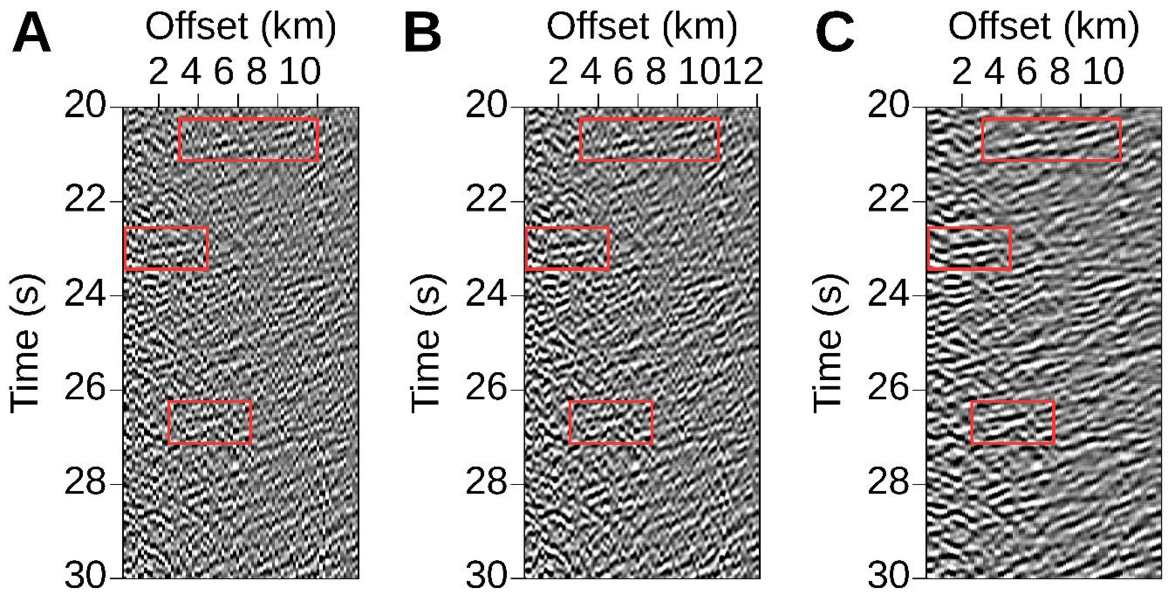

Fig. S11. Offset interpolation in common-midpoint (CMP) domain. (A) CMP gather after low frequency enhancement and linear noise removal in the shot-offset domain. The trace spacing is 150 m and the number of traces is 81. (B) The same CMP gather after interpolating the offsets to 12.5 m along the required dips (fig. S12). The number of traces is 960. (C) The offset interpolated CMP gather in (B) after normal moveout (NMO) correction with the best stacking velocities (fig. S13) and after a windowed wavenumber filter to remove the non-flat events. Red windows highlight the regions showing considerable improvements.

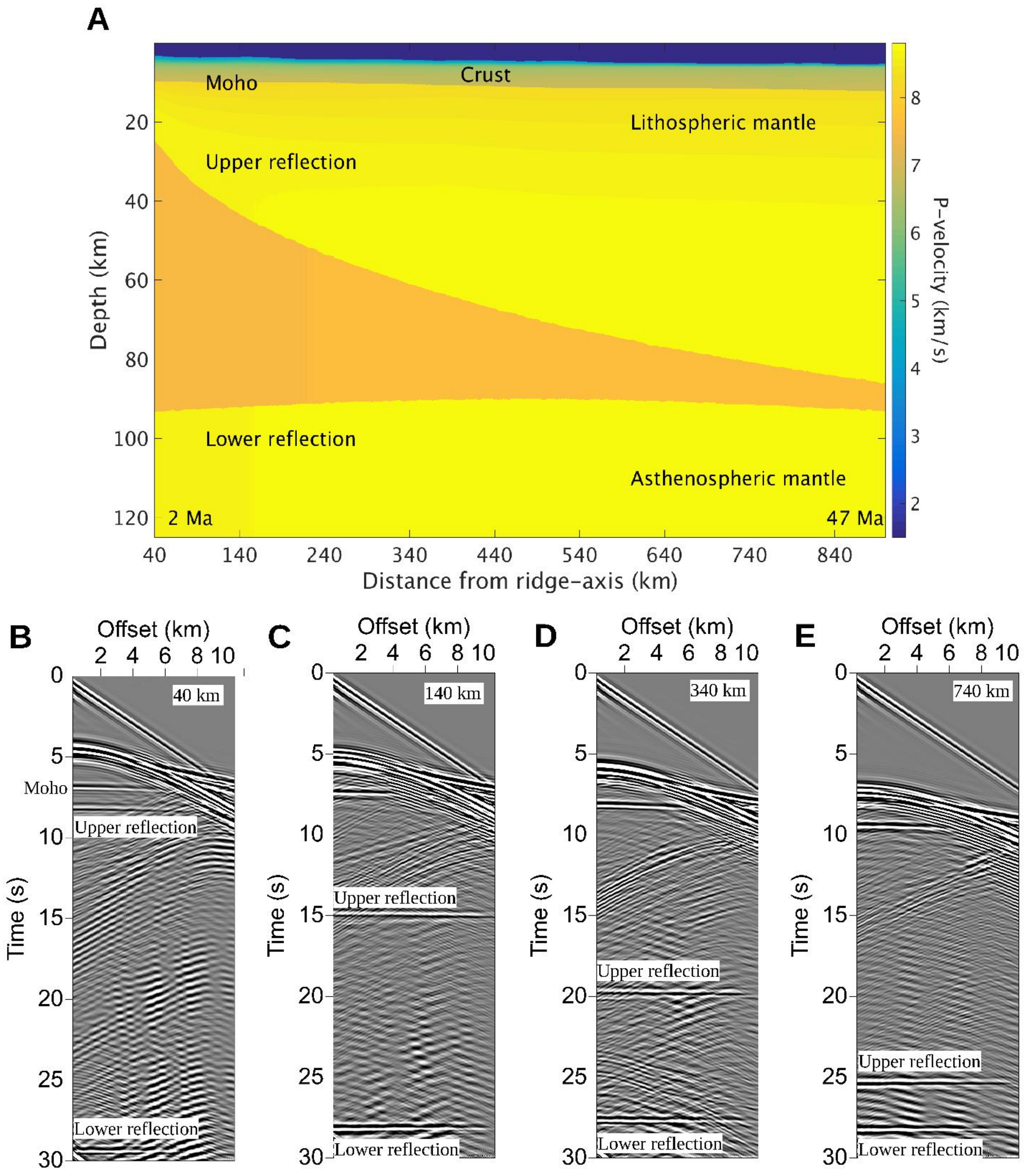

Fig. S12. Synthetic seismogram modeling to estimate the dip of the mantle reflections. (A) The P-wave velocity model used for synthetic seismogram computation (*45*) from approximately 2 Ma (40 km distance) to 47 Ma (740 km distance). The seafloor and basement topography for the model is obtained by smoothing the observed seafloor and basement topography, respectively. The upper mantle reflection represents a 10% P-wave velocity drop and follows the 1300°C from seismology studies (*46*) whereas the flatter lower reflection represents a 10% P-velocity increase. A Ricker wavelet of dominant frequency of 10 Hz is used as a source. (B) Modeled synthetic shot gather located at the left end (~40 km distance) on the P-wave velocity model. (C) Modeled synthetic shot gather located at 140 km distance. (D) Modeled synthetic shot gather located at 340 km distance. (E) Modeled synthetic shot gather located at 740 km distance.

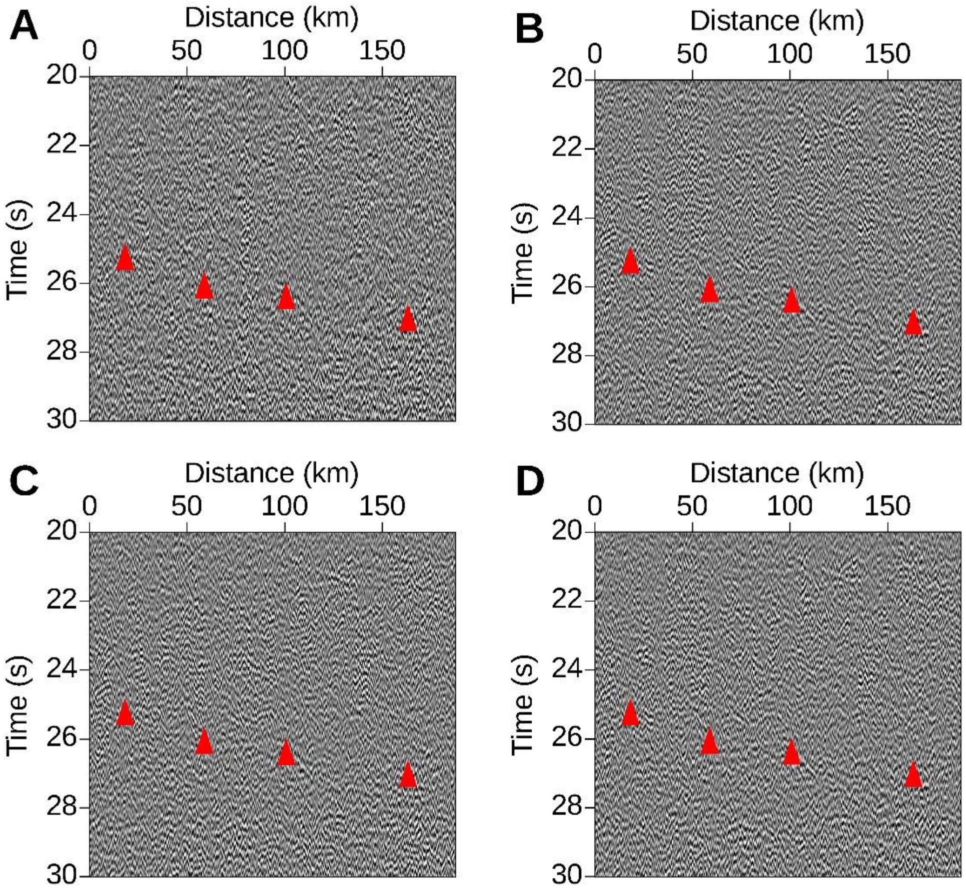

Fig. S13. Constant velocity full-offset stack sections. A stack section after Normal Move-Out (NMO) correcting the offset-interpolated CMP gathers with (A) 2.5 km/s, (B) 5 km/s, (C) 7.5 km/s and (D) 9.9 km/s stacking velocities. Red arrows mark a potential reflection, which is enhanced further.

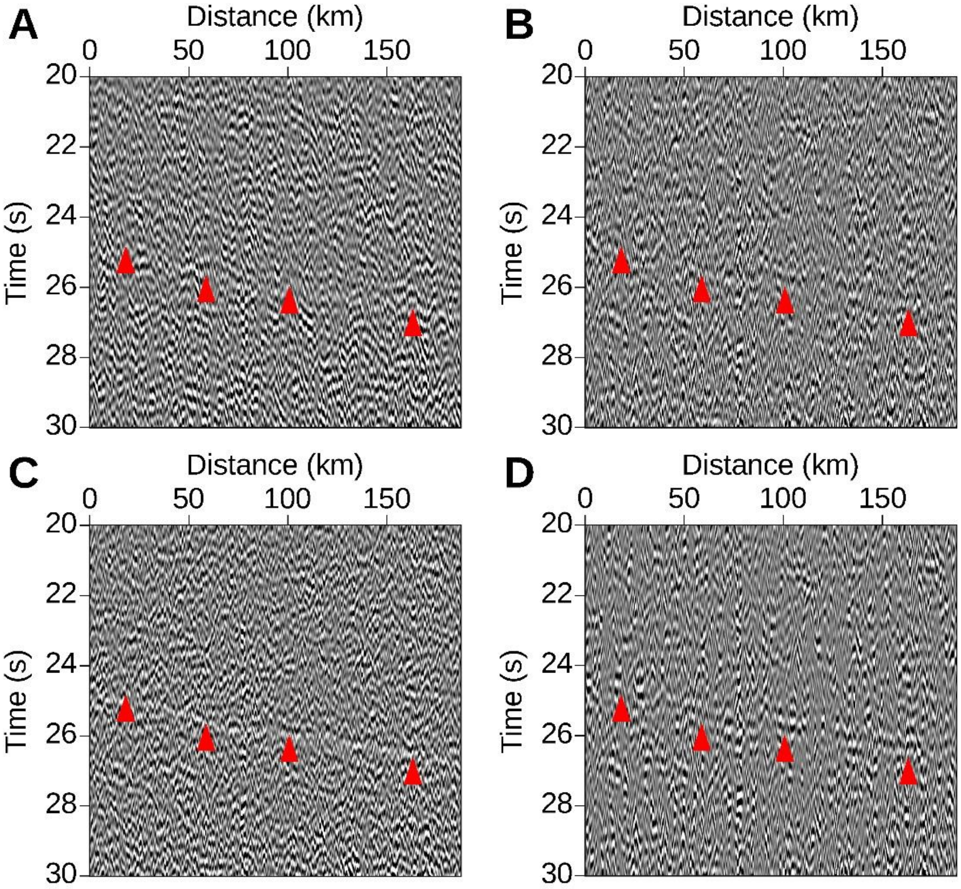

Fig. S14. Improvement in seismic image during different stages of processing. The same stack section as in fig. S13 is shown after (A) the low frequency enhancement (fig. S9) and removal of linear dipping noise in the shot-offset domain (fig. S10), (B) after (A) and further offset interpolation and enhancement of flat events in the CMP domain (fig. S11), (C) after (A), (B) and further post-stack processing and (D) after (A), (B), (C) and the application of an edge-preserving smoothing filter (*47*). The reflection, which has improved at every step, is marked by the red arrow.

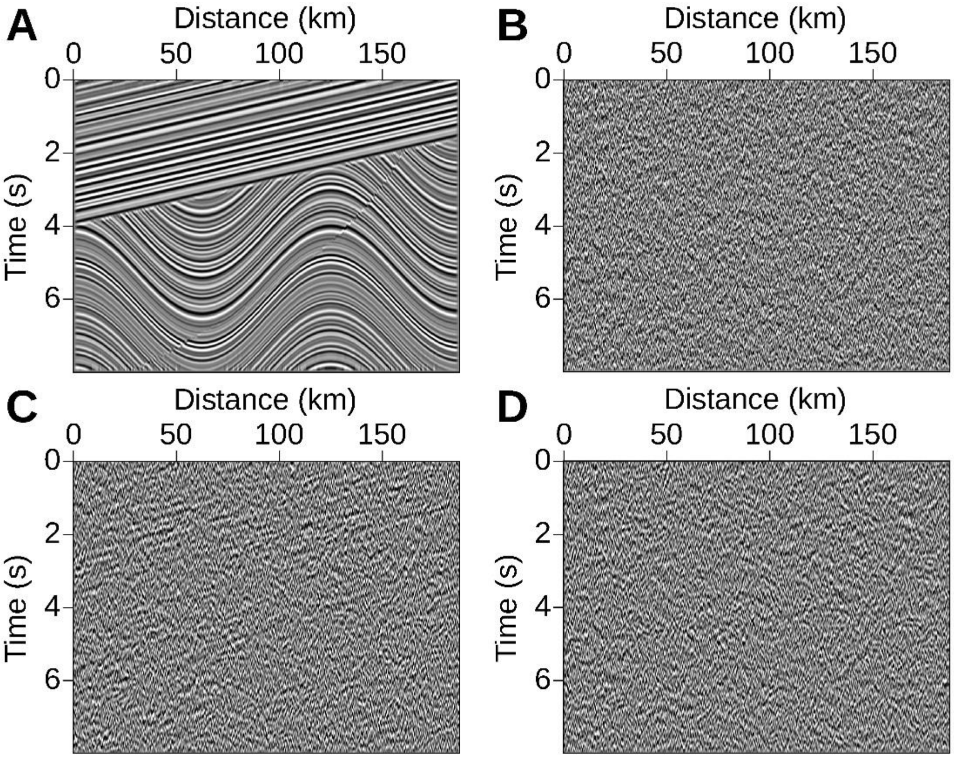

Fig. S15. Limitation of edge-preserving smoothing. (A) A sigmoid model is taken as a seismic image with both constant and rapidly changing dip patterns. (B) Sufficient gaussian noise is added to mask the pattern completely. (C) Recovered image when only constant dips corresponding to the linear pattern in (A) are searched (*47*). (D) Recovered image when all dips are searched (*47*).

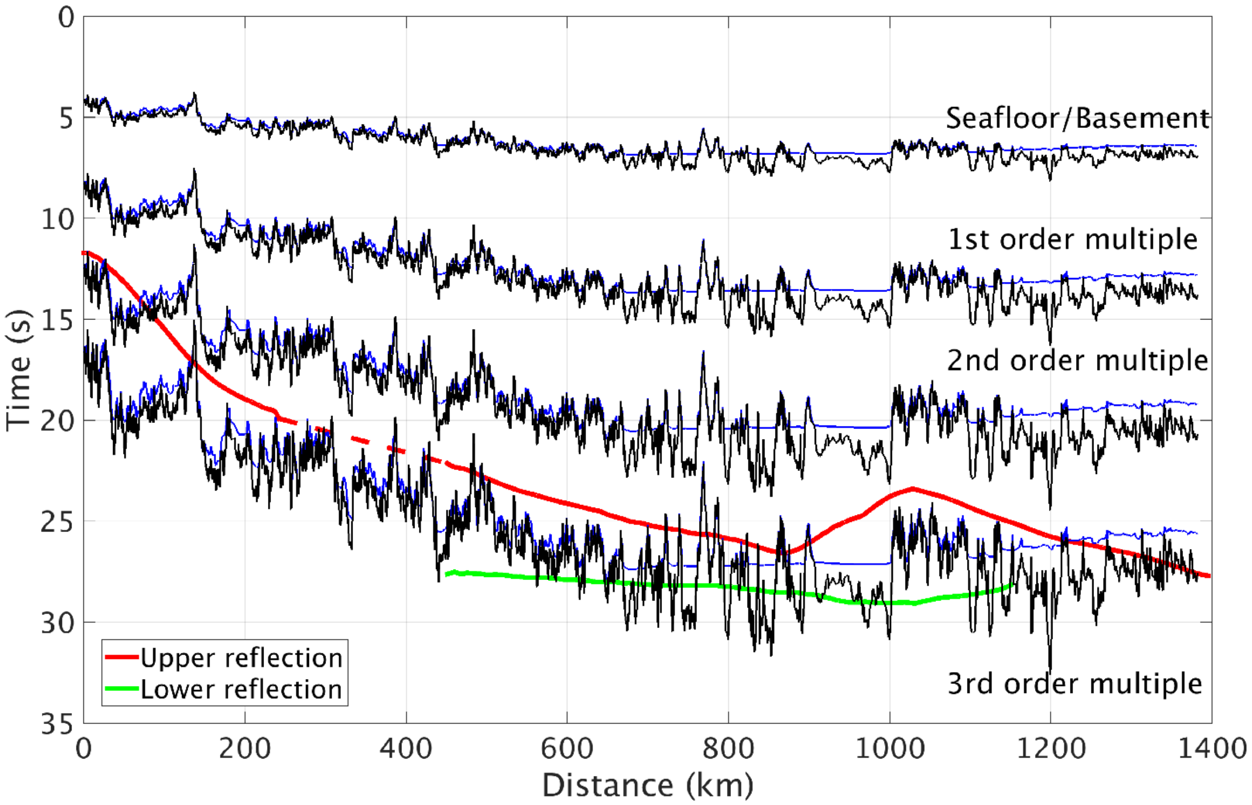

Fig. S16. Superposition of the multiples on the seismic image. The first, second and third order multiple arrivals from the seafloor (blue) and basement (black) reflections along the entire profile have been superimposed on the picked mantle reflections (Fig. 2, figs. S17-S19).

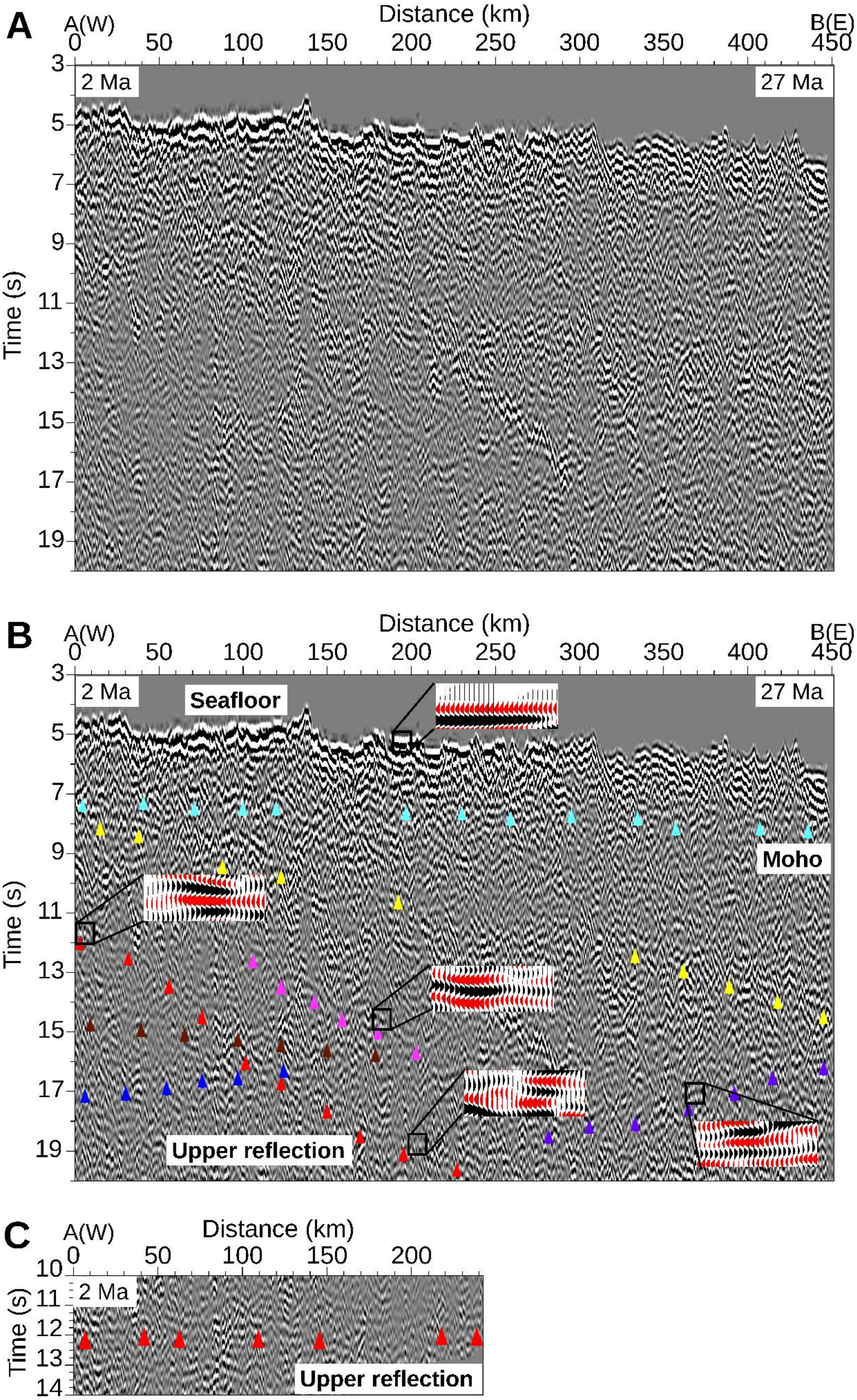
A
A(W)
Distance (km)
B(E)
0 50 100 150 200 250 300 350 400 450
3 5 7 9 11 13 15 17 19
Time (s)
2 Ma
27 Ma
B
A(W)
Distance (km)
B(E)
0 50 100 150 200 250 300 350 400 450
3 5 7 9 11 13 15 17 19
Time (s)
2 Ma
27 Ma
Seafloor
Moho
Upper reflection
C
A(W)
Distance (km)
0 50 100 150 200
10 11 12 13 14
Time (s)
2 Ma
Upper reflection

Fig. S17. Seismic image from 2 Ma to 27 Ma. (A) Uninterpreted seismic image from profile A-B (2 Ma to 27 Ma). (B) Interpreted seismic image showing the seafloor, Moho (cyan arrows), a continuous dipping 'upper reflection' (red arrows) of polarity opposite to the seafloor and a number of local events of varying dip and polarity (blue, brown, yellow, magenta and violet arrows). Inset polarity wiggle plots denote negative amplitude in red and positive amplitude in black. (C) Zoom-in of the first 250 km with the upper reflection flattened at ~11.7 s by a static time shift for a better visualization.

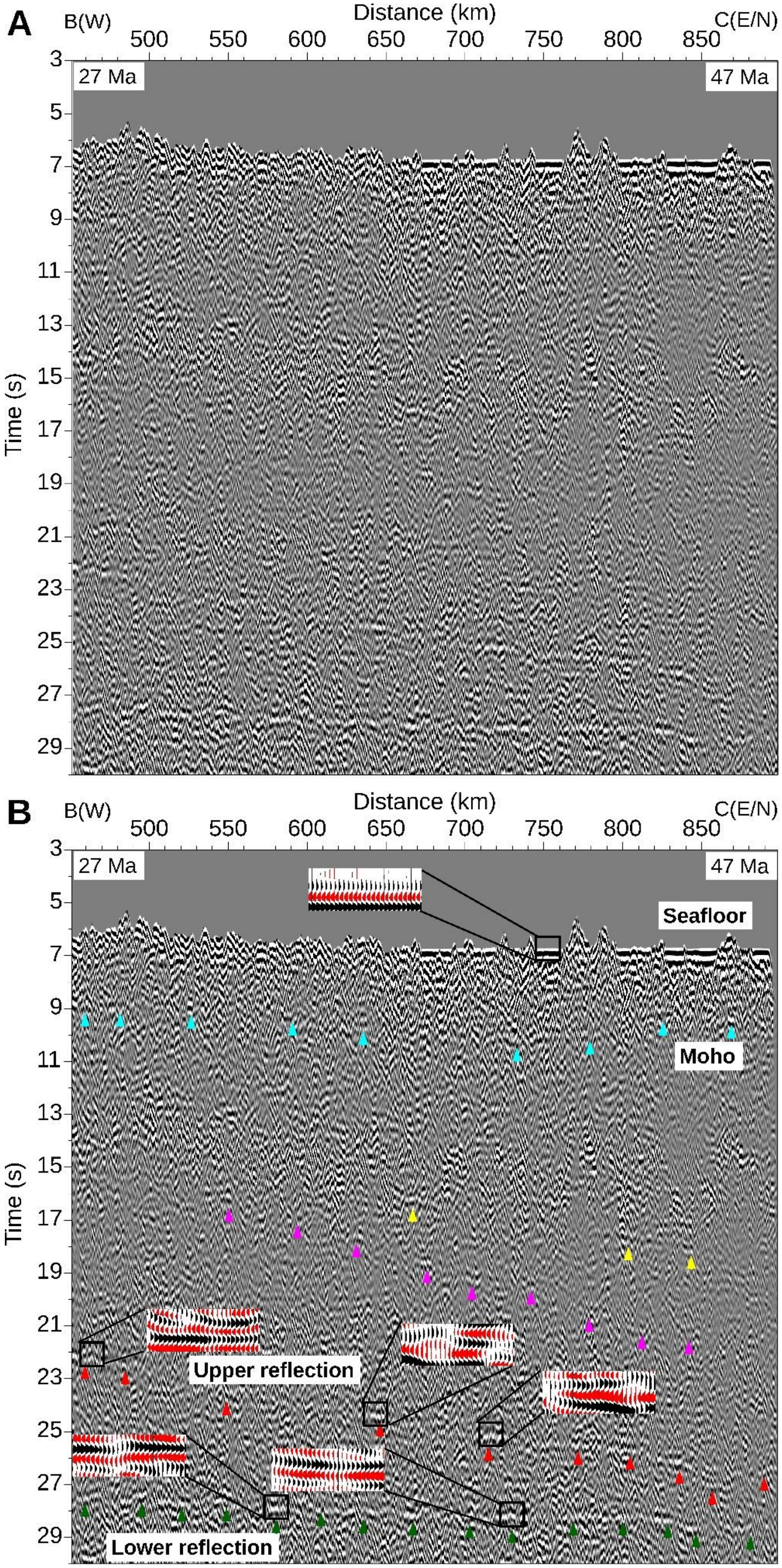
A
B(W)
Distance (km)
C(E/N)
500
550
600
650
700
750
800
850
27 Ma
47 Ma
Time (s)
3
5
7
9
11
13
15
17
19
21
23
25
27
29
B
Seafloor
Moho
Upper reflection
Lower reflection

Fig. S18. Seismic image from 27 Ma to 47 Ma. (A) Uninterpreted seismic image from profile B-C (27 Ma to 47 Ma). (B) Interpreted seismic image showing the seafloor, Moho (cyan arrows), the upper reflection which has polarity opposite to the seafloor (red arrows) and dipping from 22 s at 27 Ma (point B) to 26 s at 47 Ma (point C). Another prominent reflection, labeled as 'lower reflection' is seen to be gently dipping around 28 s (green arrows) which can be followed throughout 27 Ma to 47 Ma and mostly having polarity opposite to the seafloor. Magenta and yellow arrows represent some other events which are not interpreted here. Inset polarity wiggle plots denote negative amplitude in red and positive amplitude in black.

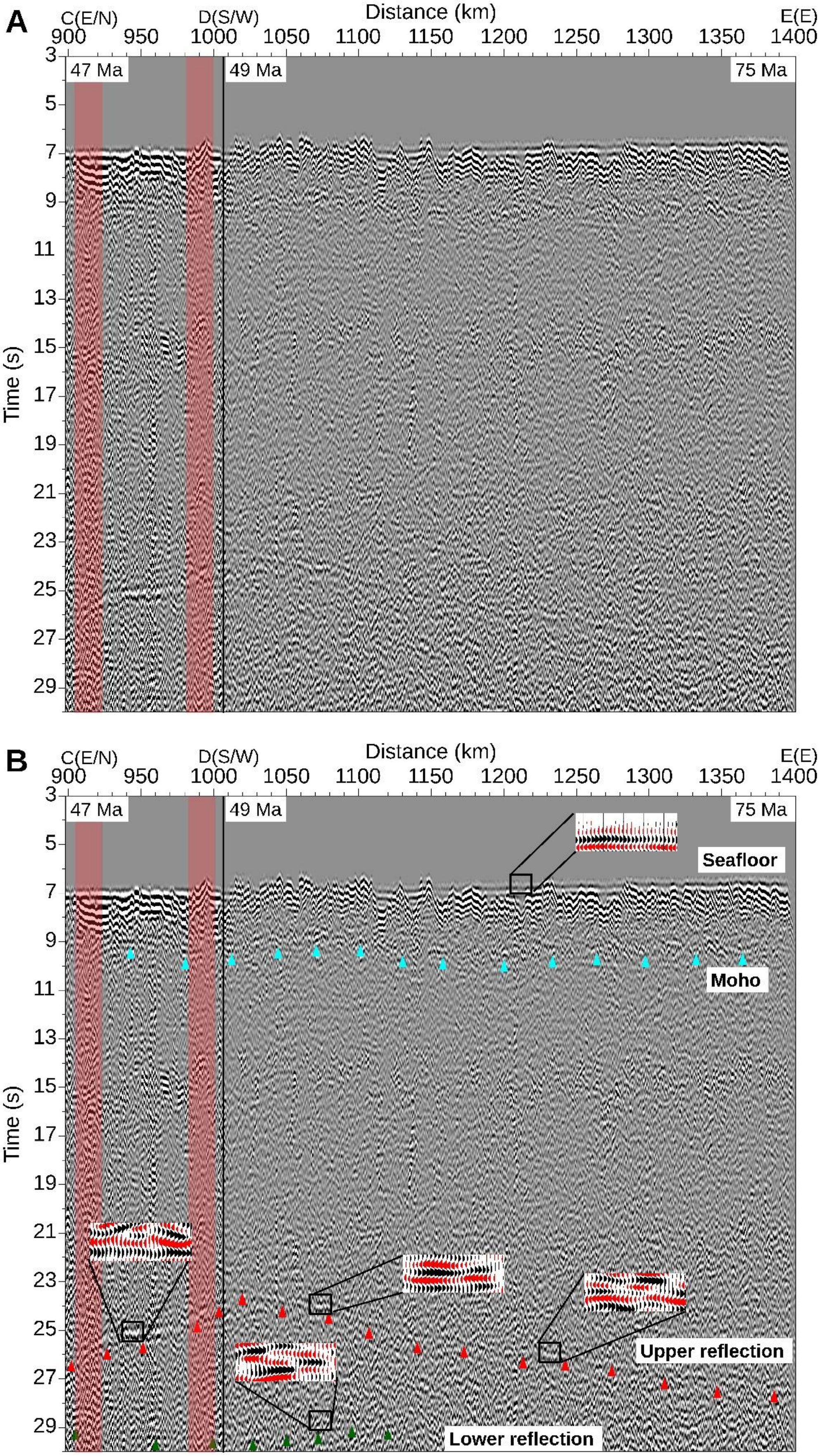
A
C(E/N)
D(S/W)
Distance (km)
E(E)
900
950
1000
1050
1100
1150
1200
1250
1300
1350
1400
Time (s)
3
5
7
9
11
13
15
17
19
21
23
25
27
29
47 Ma
49 Ma
75 Ma
B
Seafloor
Moho
Upper reflection
Lower reflection

Fig. S19. Seismic image from 47 Ma to 75 Ma. (A) Uninterpreted seismic image from profile C-E consisting of a ridge-parallel isochrone line from 47 Ma to 49 Ma (profile C-D) and the ridge-perpendicular flowline from 49 Ma to 75 Ma (profile D-E). The turning point is marked by vertical black solid line at point D. The red shaded regions indicate the approximate intersection of the second-order discontinuities (fig. S1) with the profile. (B) Interpreted seismic image with the upper reflection, marked by red arrows, can be seen to continue from fig. S18 at 26 s (point C, 47 Ma), however instead of dipping towards older ages like previously, is observed to shallow to 25 s at ~950 km distance and then further to 24 s at 1007 km distance (point D, 49 Ma). This further continues dipping towards older ages reaching ~27 s at the end of the profile (point E, 75 Ma). The lower reflection can also be traced in continuity with fig. S18 at ~29 s at 47 Ma (point C) and dipping slightly until point 49 Ma (point D), before gently shallowing back to ~29 s at 1130 km distance (58 Ma). Note the turning noise of the ship obscures imaging of the reflections near points C (47 Ma) and D (49 Ma). Inset polarity wiggle plots denote negative amplitude in red and positive amplitude in black.

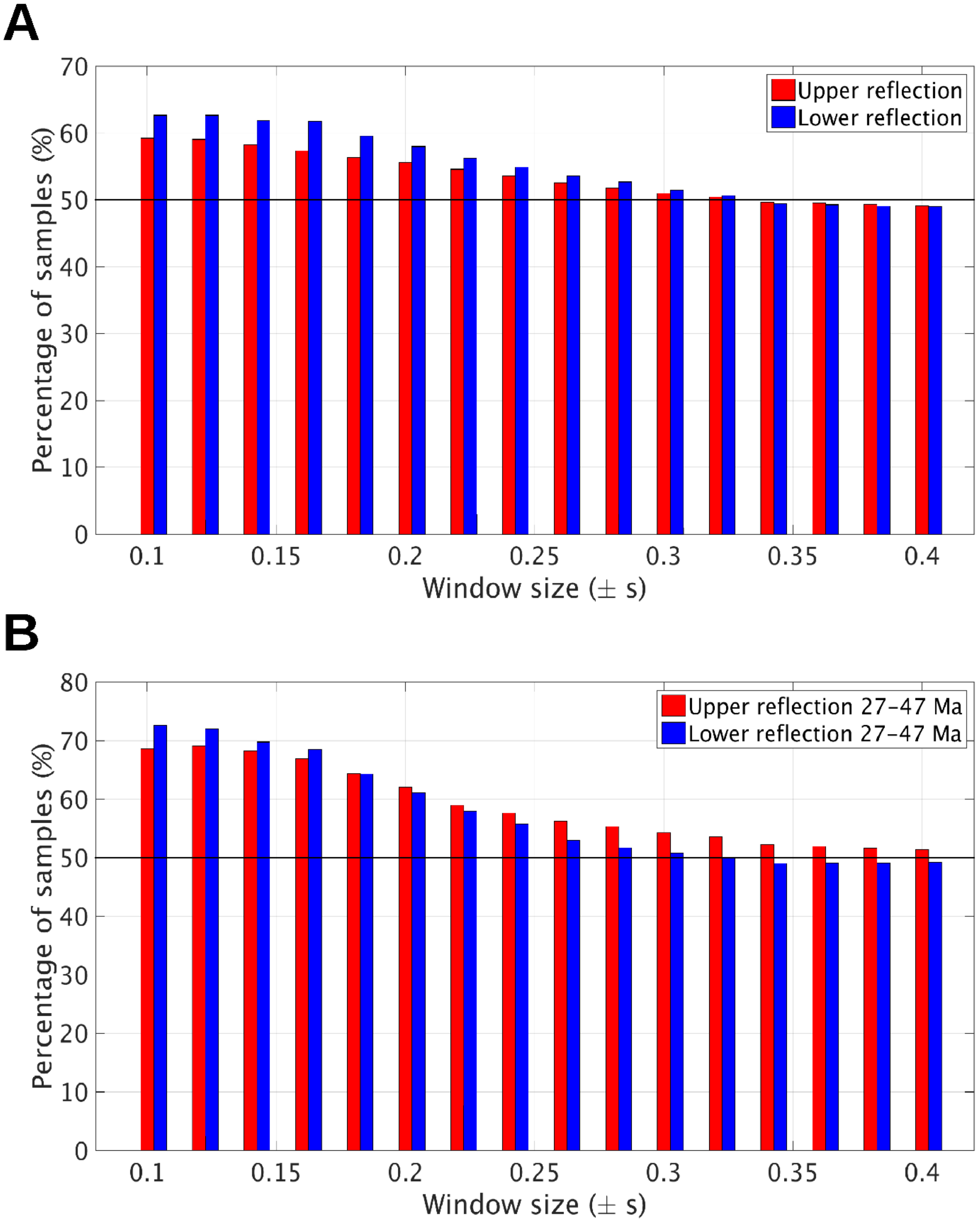

Fig. S20. Polarity analysis of the mantle reflections. (A) Percent of samples having a maximum negative amplitude as a function of window width (in seconds) of the picked upper reflection from 2 Ma to 75 Ma and the picked lower reflection from 27 Ma to 58 Ma (Fig. 2, figs. S17-S19). (B) The same as (A) except only for 27 Ma to 47 Ma (fig. S18) where the lower reflection is best imaged. The black horizontal line indicates the threshold of 50%.

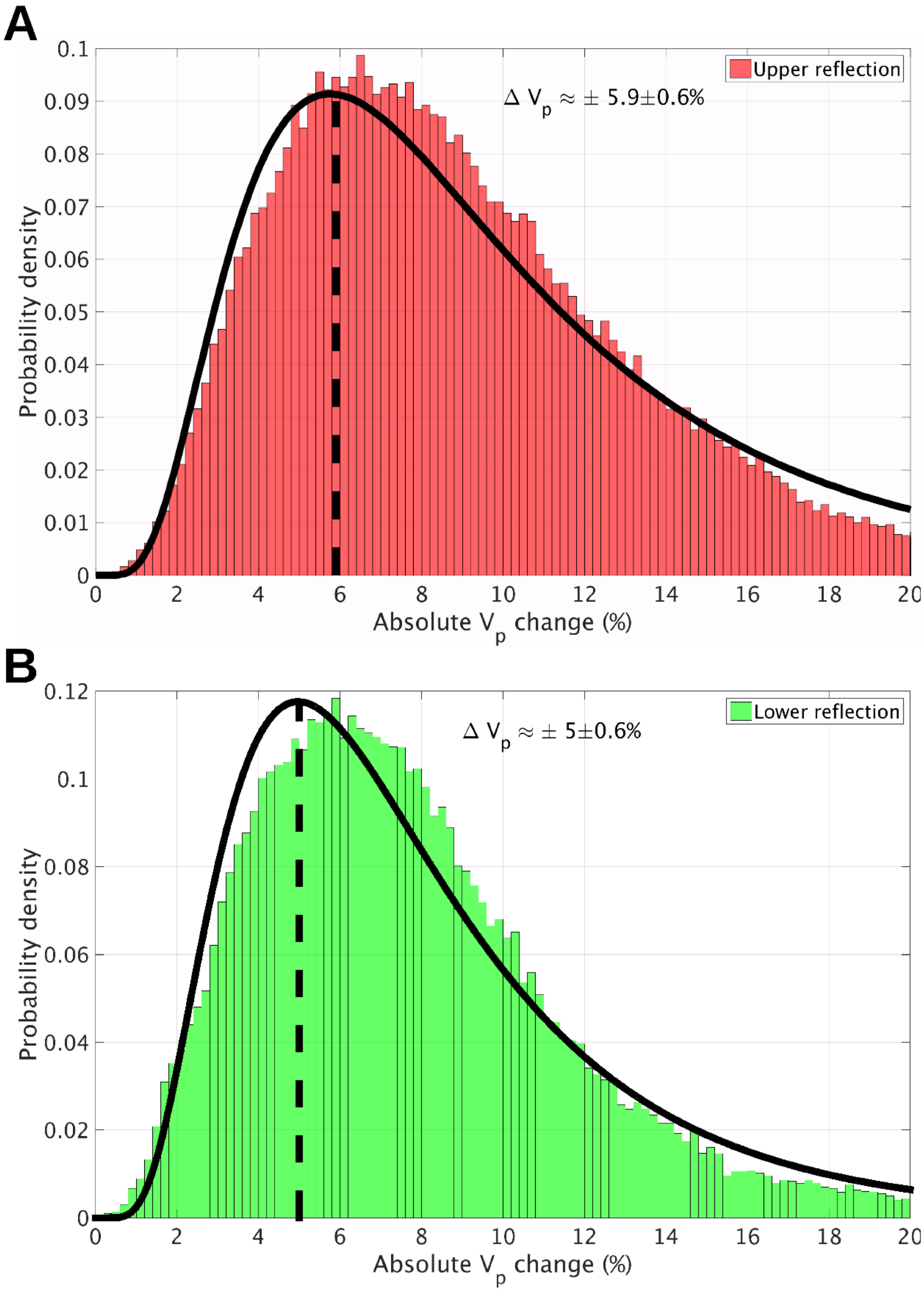

Fig. S21. Percent P-wave velocity drop across the mantle reflections. (A) Histogram representing the absolute percent P-wave velocity change for the upper reflection from 2 Ma to 75 Ma (*13*,*18*). The thick black line corresponds to the best-fitting log normal curve with the vertical dashed black line indicating the mode value of the curve. (B) Same representation but for the lower reflection from 27 Ma to 58 Ma.

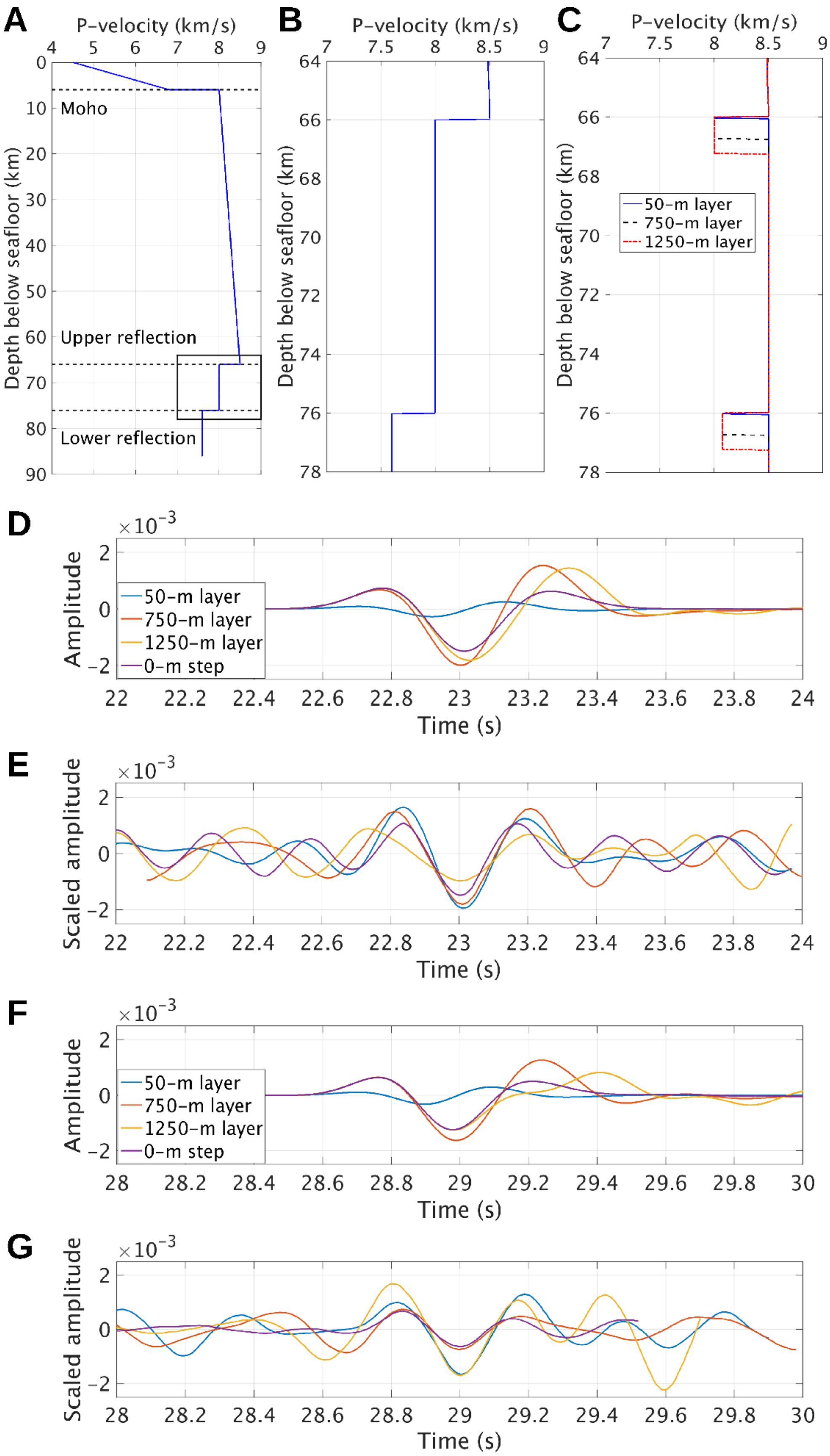
A
P−velocity (km/s)
4 5 6 7 8 9
Depth below seafloor (km)
0 10 20 30 40 50 60 70 80 90
Moho
Upper reflection
Lower reflection
B
P−velocity (km/s)
7 7.5 8 8.5 9
Depth below seafloor (km)
64 66 68 70 72 74 76 78
C
P−velocity (km/s)
7 7.5 8 8.5 9
Depth below seafloor (km)
64 66 68 70 72 74 76 78
50−m layer
750−m layer
1250−m layer
D
×10^{-3}
Amplitude
2 0 −2
50−m layer
750−m layer
1250−m layer
0−m step
22 22.2 22.4 22.6 22.8 23 23.2 23.4 23.6 23.8 24
Time (s)
E
×10^{-3}
Scaled amplitude
2 0 −2
22 22.2 22.4 22.6 22.8 23 23.2 23.4 23.6 23.8 24
Time (s)
F
×10^{-3}
Amplitude
2 0 −2
50−m layer
750−m layer
1250−m layer
0−m step
28 28.2 28.4 28.6 28.8 29 29.2 29.4 29.6 29.8 30
Time (s)
G
×10^{-3}
Scaled amplitude
2 0 −2
28 28.2 28.4 28.6 28.8 29 29.2 29.4 29.6 29.8 30
Time (s)

Fig. S22. Synthetic seismogram modeling. (A) Full 1-D P-velocity-depth profile used for synthetic seismogram modeling (*45*). The black rectangle shows a blow-up in panels (B) and (C). (B) A 0-m step model in which velocities across the upper and lower reflections decrease sharply. (C) A 50-1250 m thick layer model with normal mantle velocities in between the reflections. (D) Modeled zero-offset waveforms for the upper reflection. (E) Observed waveforms for the upper reflection. (F) Modeled zero-offset waveforms for the lower reflection. (G) Observed waveforms for the lower reflection.

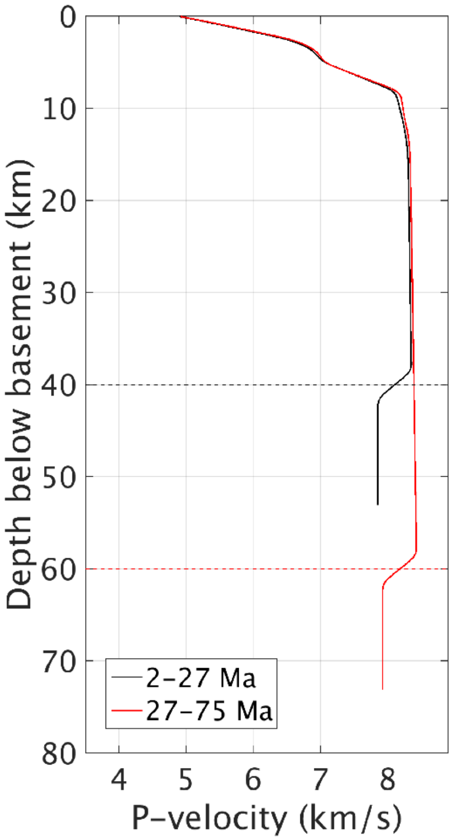

Fig. S23. 1-D P-wave velocity model for the depth conversion. Crustal and upper mantle P-wave velocities taken from a co-located wide-angle tomography from 0 Ma to 27 Ma (*50*). The black curve represents the velocity profile for 2 Ma to 27 Ma and the red curve represents the velocity profile for 27 Ma to 75 Ma. The dashed lines indicate the P-wave velocity drop across the upper mantle reflection (fig. S21) and shown here at 40 km for 2 Ma to 27 Ma and at 60 km for 27 Ma to 75 Ma.

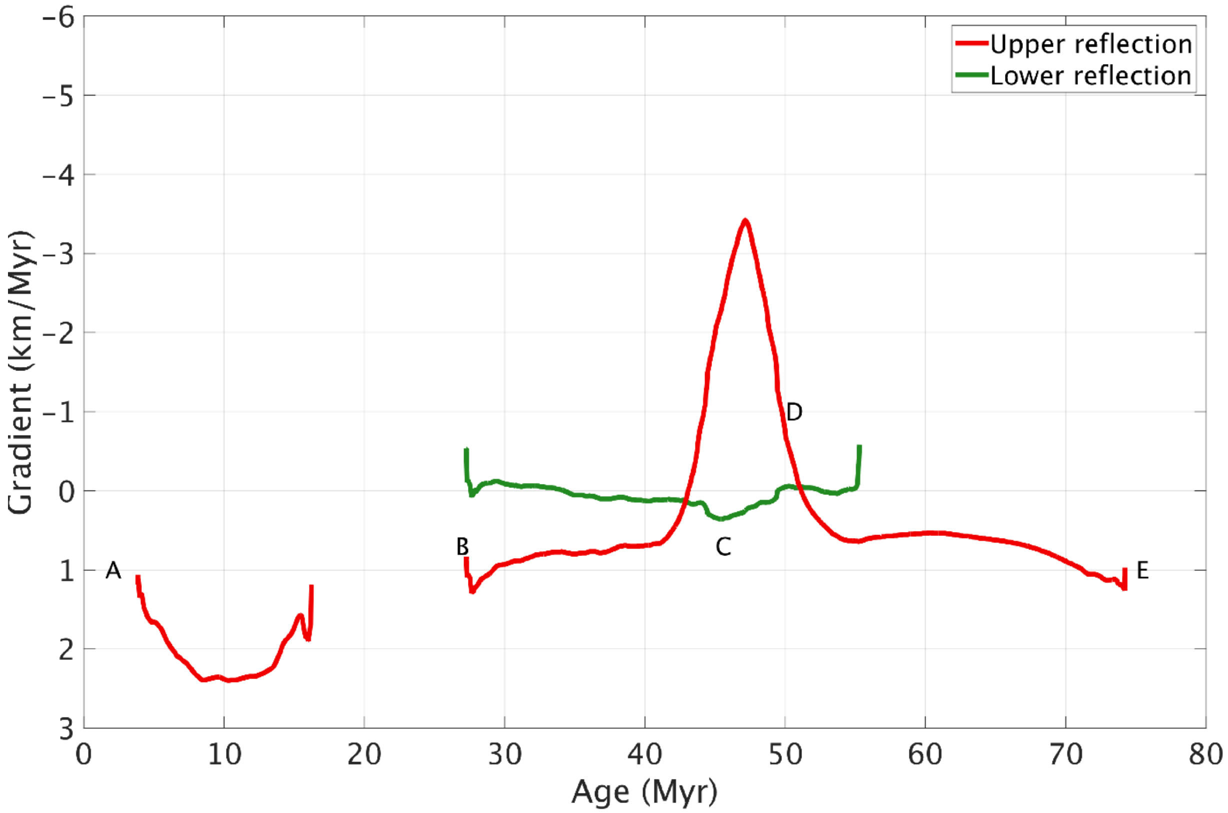

Fig. S24. The dip of depth converted reflections. Variation of the dip of the upper (red) and lower (green) reflections with age. Points A-E along the profile are the same as marked in Figs. 1-3 and figs. S17-S19.

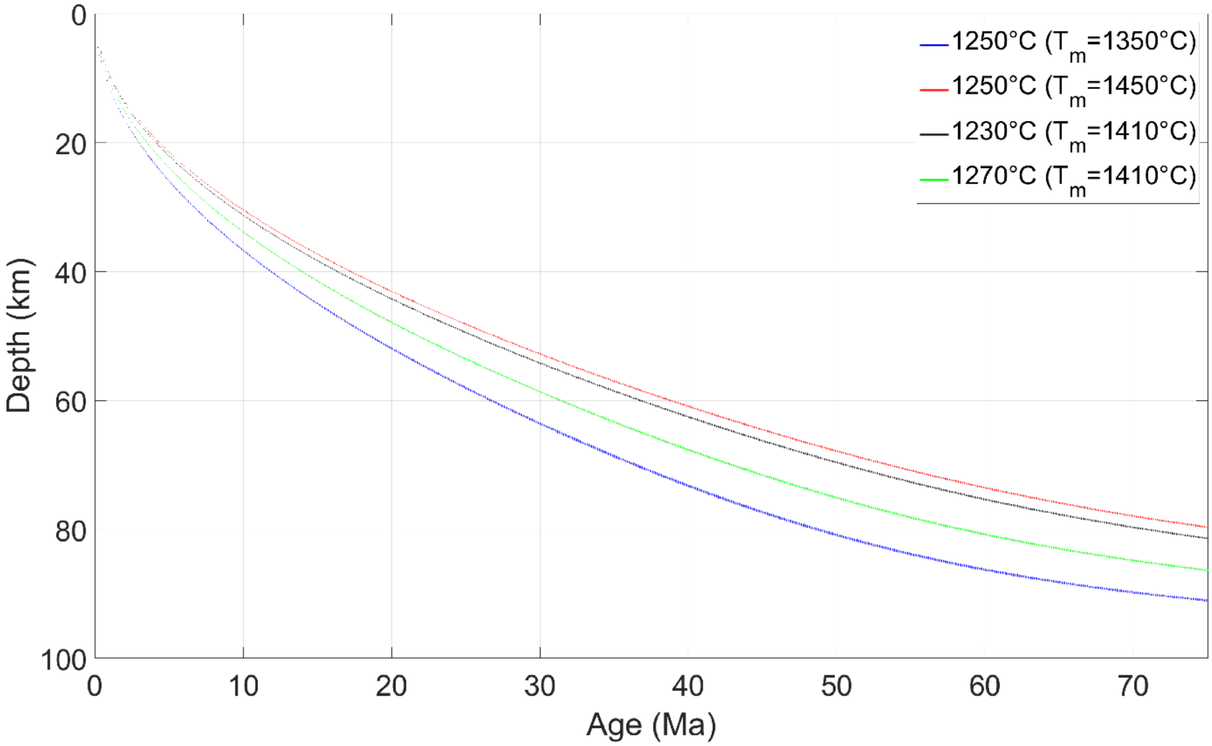

Fig. S25. Thermal modeling uncertainty. Effect of mantle temperature (T_m) range of 1350-1450°C (*56*) on the thermal modeling estimate of 1250° C and an uncertainty of 20°C, with respect to mantle temperature of 1410°C (*25*).

A

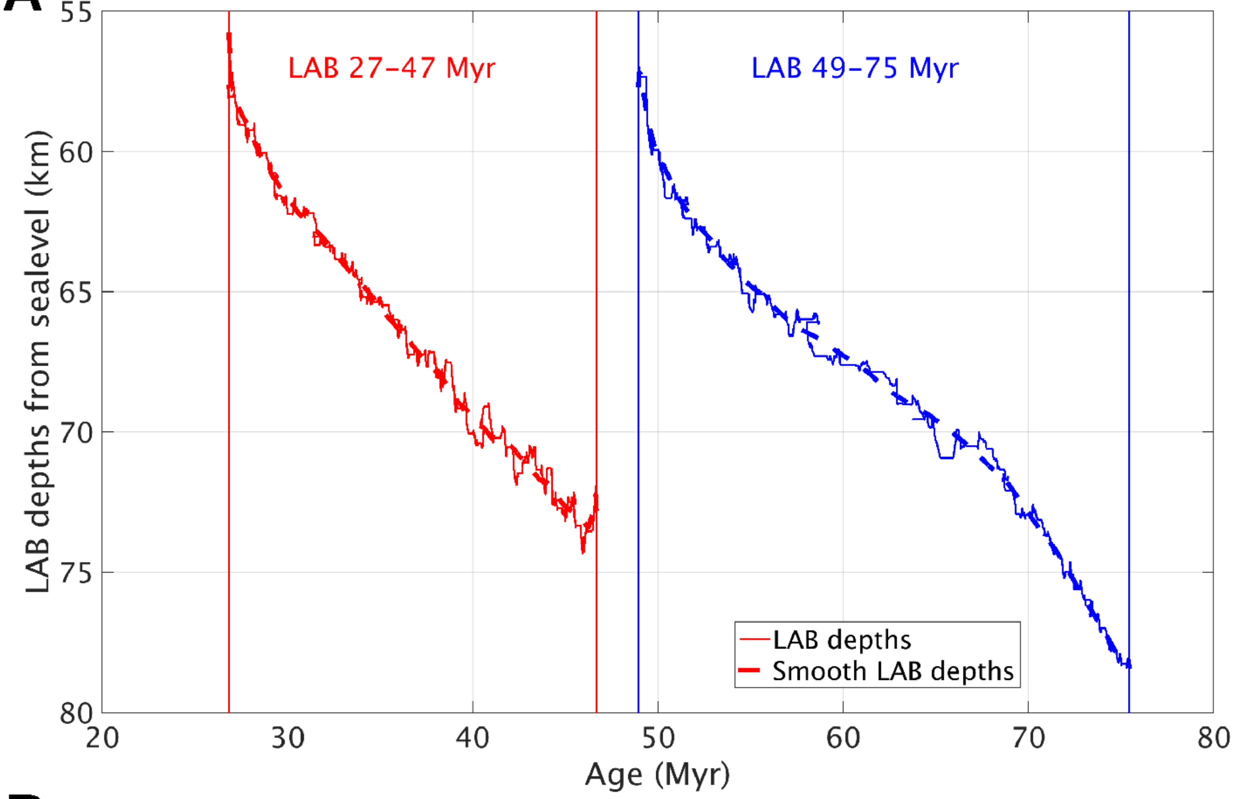

LAB 27-47 Myr
LAB 49-75 Myr
LAB depths from sealevel (km)
55
60
65
70
75
80
20
30
40
50
60
70
80
Age (Myr)
LAB depths
Smooth LAB depths

B

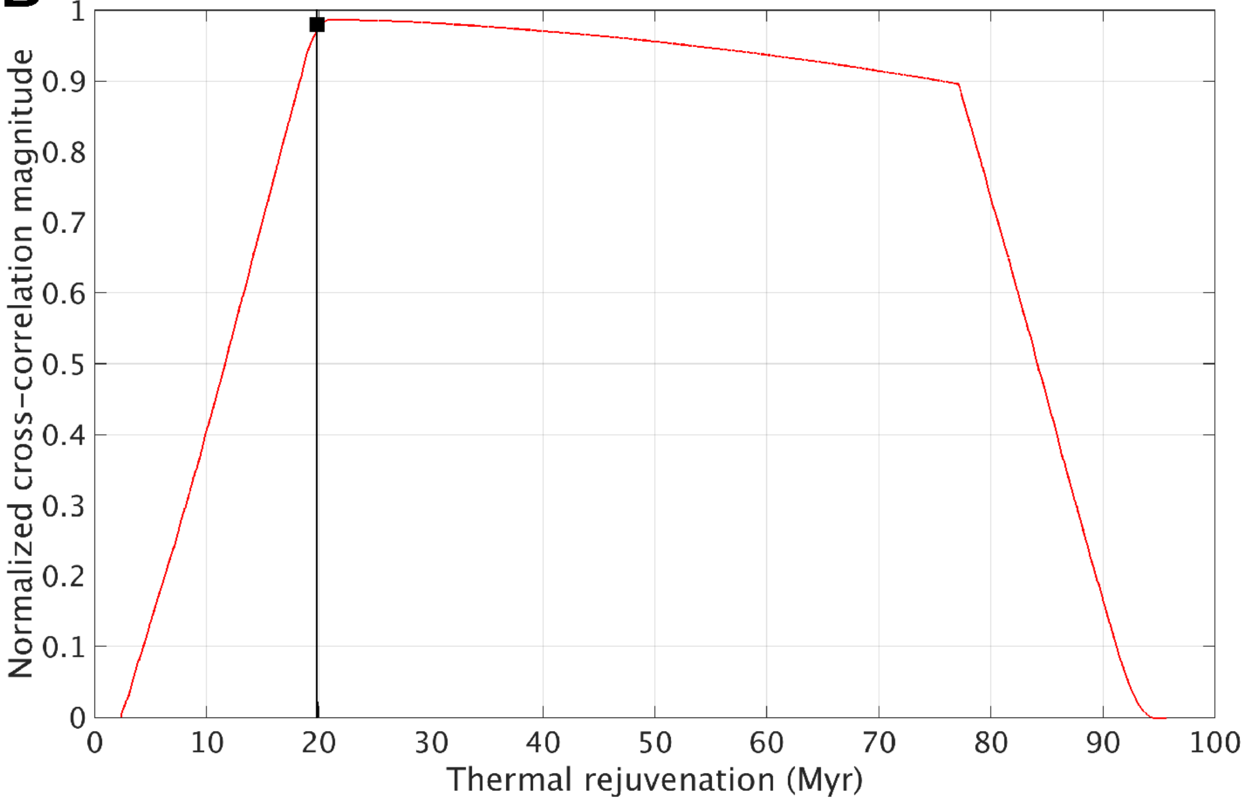

Normalized cross-correlation magnitude
1
0.9
0.8
0.7
0.6
0.5
0.4
0.3
0.2
0.1
0
0
10
20
30
40
50
60
70
80
90
100
Thermal rejuvenation (Myr)

Fig. S26. Thermal rejuvenation age of the LAB from cross-correlation. (A) Variation of LAB depths with age for two distinct segments: B-C (red) and D-E (blue). (B) Cross-correlation of the D-E (blue) LAB depth with B-C (red) LAB depth in (A). The black square denotes the peak of the cross-correlation and the black vertical line represents the rejuvenation age at which the peak is observed.

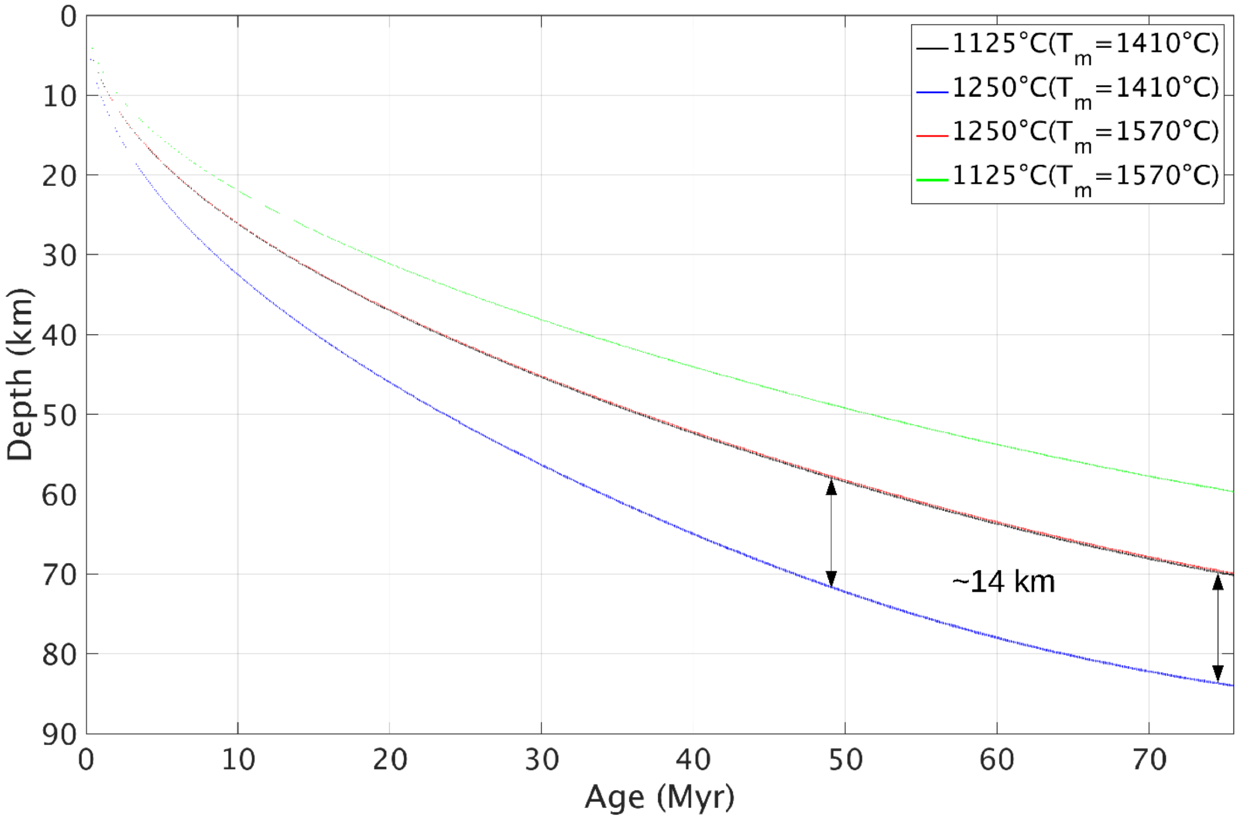

Fig. S27. Mantle potential temperatures (T_m). 1125ºC (black/green) and 1250ºC (red/blue) isotherms have been plotted for a regular mantle (*1*) having a mantle potential temperature of 1410ºC (black/blue) (*25*) and a relatively hotter mantle having a mantle potential temperature of 1570ºC (red/green), demonstrating that the 1125ºC isotherm at a regular mantle temperature could associated with the 1250ºC isotherm for higher mantle temperature caused by mantle thermal anomaly.

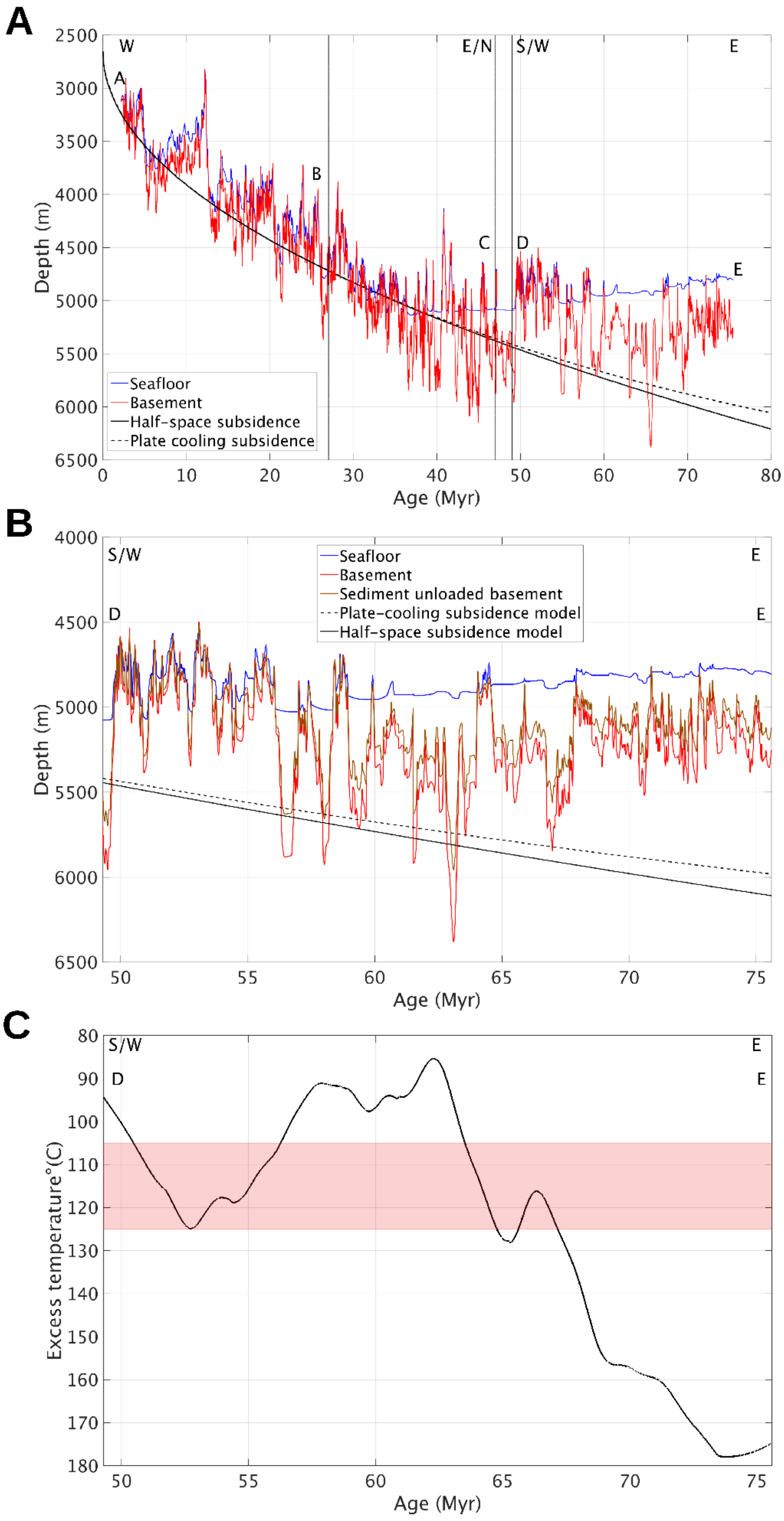
A
2500
3000
3500
4000
4500
5000
5500
6000
6500
Depth (m)
0
10
20
30
40
50
60
70
80
Age (Myr)
W
E/N
S/W
E
A
B
C
D
E
Seafloor
Basement
Half-space subsidence
Plate cooling subsidence
B
4000
4500
5000
5500
6000
6500
Depth (m)
50
55
60
65
70
75
Age (Myr)
S/W
E
D
E
Seafloor
Basement
Sediment unloaded basement
Plate-cooling subsidence model
Half-space subsidence model
C
80
90
100
110
120
130
140
150
160
170
180
Excess temperature°(C)
50
55
60
65
70
75
Age (Myr)
S/W
E
D
E

Fig. S28. Basement uplift and excess mantle temperature. (A) Seafloor (blue) and basement (red) interfaces picked from the seismic image (Fig. 2, figs. S17-S19) and depth converted. Dashed black and solid black lines represent the plate-cooling and half-space subsidence with ridge-axis depth from Audhkhasi and Singh (*54*). (B) Zoom-in over the easternmost segment of the profile (D-E) (49 Ma to 75 Ma) in (A) to highlight the basement uplift. Additionally, a sediment unloaded basement (*55*) has been plotted (brown curve), which has been used to compute the uplift with respect to the subsidence models. (C) Estimation of excess mantle temperature (*57*) in the asthenosphere channel (*56*) to cause the observed uplift in (B) and its variation along D-E. The red shaded region represents the mean of the computed excess mantle temperature.

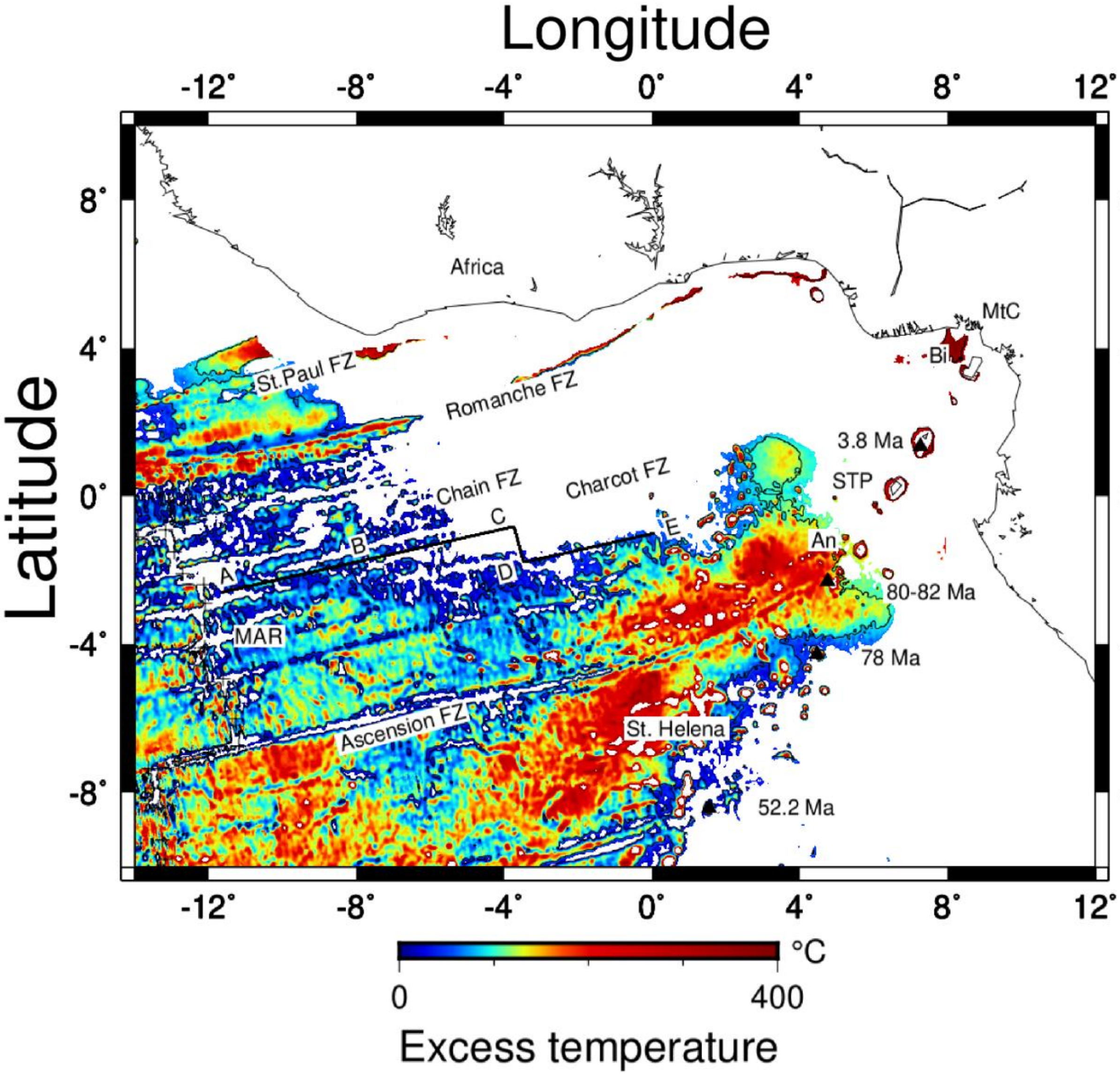

Fig. S29: Regional excess mantle temperature. Excess mantle temperature computations extended to the whole region using global datasets (*14*,*27*). Our seismic profile is shown in black along A-E. Thin black contour lines denote 200°C excess temperature.

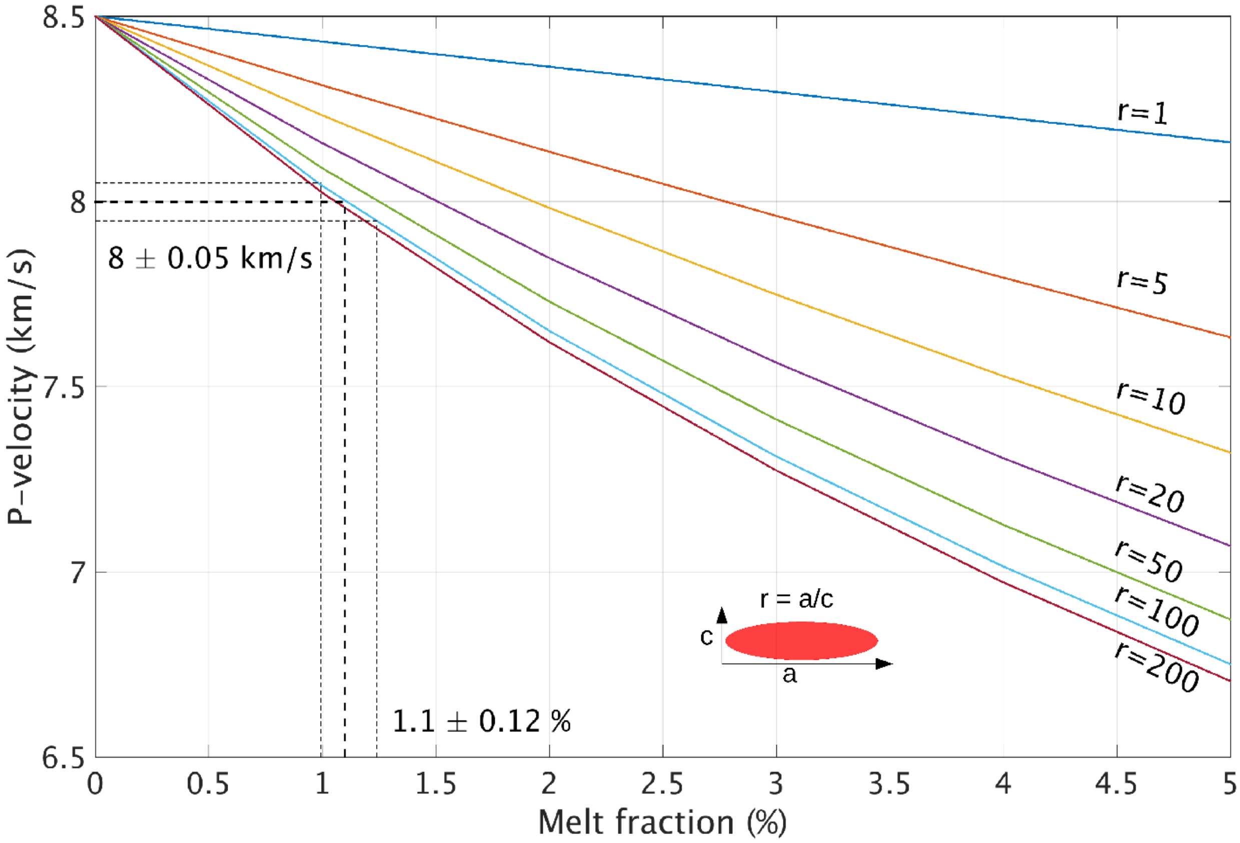

Fig. S30. Melt content at the LAB. Effect of increasing melt content on the P-wave velocity of mantle peridotite is modeled as a function of aspect ratio (r, inset red ellipse) of the pore spaces (*58*). a and c are major and minor axes of ellipsoid melt inclusion. The thick black dashed lines represent the P-wave velocity just below the LAB after the P-wave velocity drop (figs. S21, S23) and the corresponding melt content for an aspect ratio of 1:100. The thin black dashed lines represent the uncertainty bounds in the P-wave velocity and the melt content estimates.

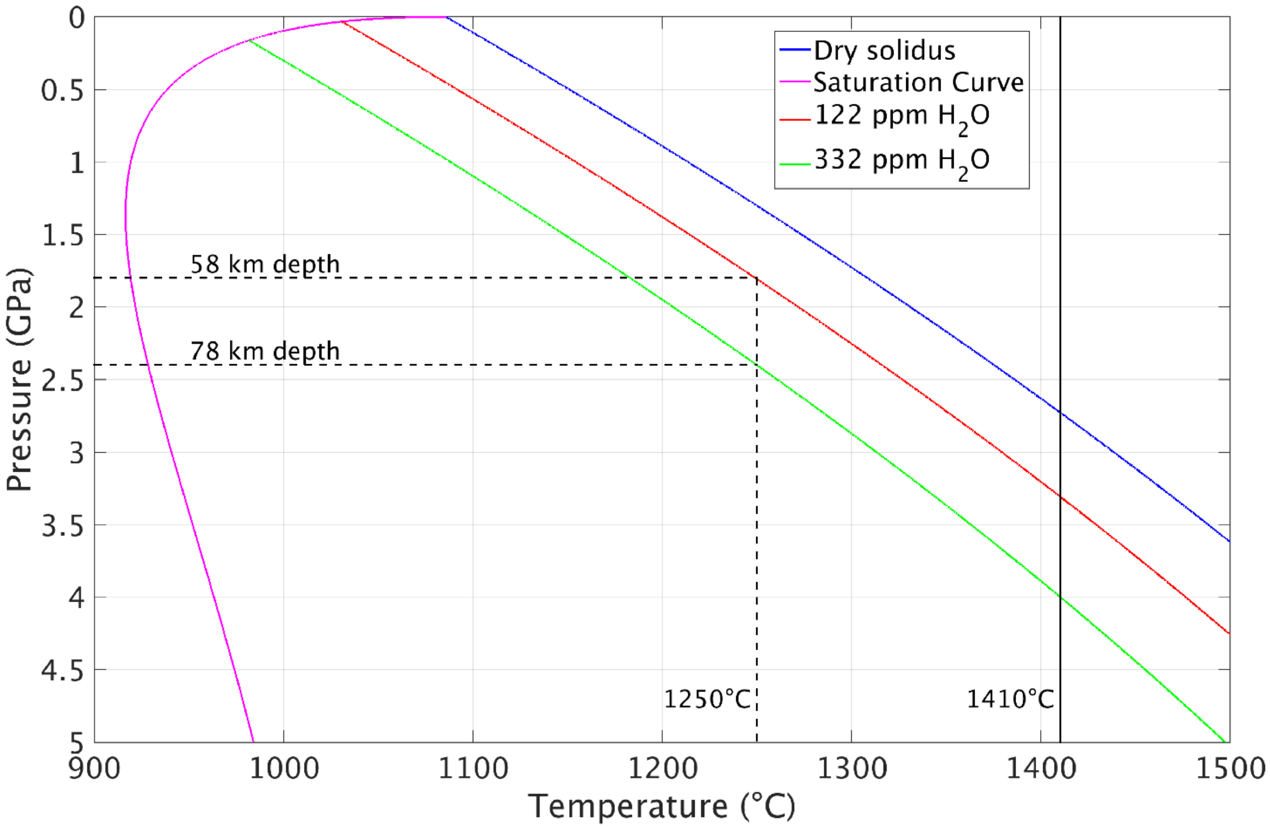

Fig. S31. Water content. The water is needed for the stability of the melt (*31*) at depths of the observed reflection and corresponding to the melt content of ~1.1% (fig. S30). Blue curve represents the dry solidus of olivine and the magenta curve represents the liquidus temperature. The solid black vertical line represents the limit of mantle temperature as 1410ºC (*25*). The dashed black horizontal lines represent the LAB depths beyond 27 Ma and the dashed black vertical line represents the LAB temperature (1250ºC). The red and green curves represent the estimated solidus curves corresponding to a water saturation of 122 and 332 ppm, respectively.